

⌚The Building Blocks of Northern Hemisphere Wintertime Stationary Waves⌚

CHAIM I. GARFINKEL AND IAN WHITE

Fredy & Nadine Herrmann Institute of Earth Sciences, The Hebrew University of Jerusalem, Jerusalem, Israel

EDWIN P. GERBER

Courant Institute of Mathematical Sciences, New York University, New York City, New York

MARTIN JUCKER

Climate Change Research Center and ARC Centre of Excellence for Climate Extremes, University of New South Wales, Sydney, Australia

MORAN EREZ

Fredy & Nadine Herrmann Institute of Earth Sciences, The Hebrew University of Jerusalem, Jerusalem, Israel

(Manuscript received 5 March 2019, in final form 2 January 2020)

ABSTRACT

An intermediate-complexity moist general circulation model is used to investigate the forcing of stationary waves in the Northern Hemisphere boreal winter by land-sea contrast, horizontal heat fluxes in the ocean, and topography. The additivity of the response to these building blocks is investigated. In the Pacific sector, the stationary wave pattern is not simply the linear additive sum of the response to each forcing. In fact, over the northeast Pacific and western North America, the sum of the responses to each forcing is actually opposite to that when all three are imposed simultaneously due to nonlinear interactions among the forcings. The source of the nonlinearity is diagnosed using the zonally anomalous steady-state thermodynamic balance, and it is shown that the background-state temperature field set up by each forcing dictates the stationary wave response to the other forcings. As all three forcings considered here strongly impact the temperature field and its zonal gradients, the nonlinearity and nonadditivity in our experiments can be explained, but only in a diagnostic sense. This nonadditivity extends up to the stratosphere, and also to surface temperature, where the sum of the responses to each forcing differs from the response if all forcings are included simultaneously. Only over western Eurasia is additivity a reasonable (though not perfect) assumption; in this sector land-sea contrast is most important over Europe, while topography is most important over western Asia. In other regions, where nonadditivity is pronounced, the question of which forcing is most important is ill-posed.

1. Introduction

Although the solar forcing at the top of the atmosphere is zonally symmetric when averaged over a day or longer, the climate of Earth is decidedly not zonally

symmetric. These zonal asymmetries, or stationary waves, are forced by asymmetries in the lower boundary, such as the land-ocean distribution and orography. The land-ocean distribution directly impacts the distribution of surface temperature and moisture, while mountains directly impact the atmospheric flow (e.g., Held et al. 2002).

Developing a good understanding of the mechanisms controlling the stationary waves is important for many reasons. First, the position and intensity of stationary waves strongly influence the weather and climate of Eurasia and North America. Stationary waves control, in large part, the distribution of storm tracks (e.g., Branstator 1995; Chang et al. 2002), which are closely linked to extreme wind and precipitation

⌚ Denotes content that is immediately available upon publication as open access.

⌚ Supplemental information related to this paper is available at the Journals Online website: <https://doi.org/10.1175/JCLI-D-19-0181.s1>.

Corresponding author: Chaim I. Garfinkel, chaim.garfinkel@mail.huji.ac.il

events (Shaw et al. 2016). Stationary waves also contribute to differences in surface temperature at comparable latitudes (Seager et al. 2002). Subtle shifts in stationary waves, such as those projected to occur under climate change, can lead to profound impacts on regional climate (Neelin et al. 2013; Simpson et al. 2014, 2016). To interpret and have confidence in simulated future changes in the climate of the extratropics, it is important to have a good understanding of the mechanisms for stationary waves in the current climate (Hoskins and Woollings 2015).

Since pioneering studies by Charney and Eliassen (1949) and Smagorinsky (1953), dozens of modeling studies have examined the forcings most crucial for atmospheric stationary waves, as summarized in the review article by Held et al. (2002). The vast majority of these earlier studies generated stationary waves not by imposing the land–ocean contrast directly, but rather by imposing an asymmetrical distribution of diabatic heating (Held et al. 2002). In boreal wintertime, the imposed diabatic heating turns out to be the most important ingredient for the generation of stationary waves, with eddy fluxes and orography playing smaller roles (Wang and Ting 1999; Held et al. 2002; Chang 2009), although there is sensitivity to the details of, among others, the damping, the precise form of the diabatic heating, and the low-level winds (Held and Ting 1990).¹

There is some ambiguity in these results, however: diabatic heating is dependent on the flow and thus not independent of orographic forcing [as noted by Nigam et al. (1988), Held et al. (2002), and Chang (2009)]. That is, the removal of orographic forcing acts to modify surface temperatures (Seager et al. 2002) and the heating distribution, which can then lead to a feedback on the stationary waves. The only way to assess the full impact of the removal of orography involves simulating how the diabatic heating may respond (Nigam et al. 1986, 1988). Similarly, diabatic heating regulates the response to orography: Ringler and Cook (1999) and Ting et al. (2001) found that diabatic heating modifies the flow incident on the mountains and alters the stationary wave generated by the mountains. A model that imposes diabatic heating independently from orographic effects cannot capture such a nonlinear effect.

An alternate class of models that has been used to study the generation of stationary waves are models in which diabatic processes are parameterized by the

model and can therefore interact with one another and with topography (e.g., Manabe and Terpstra 1974; Blackmon et al. 1987; Broccoli and Manabe 1992; Kitoh 1997; Inatsu et al. 2002; Wilson et al. 2009; Brayshaw et al. 2009, 2011; Saulière et al. 2012; White et al. 2017). Large-scale orography (in particular the Rockies and Tibetan Plateau) has been found in many of these studies to be the dominant contributor to stationary waves. Land–sea contrast was found to be of secondary importance in forcing stationary waves, by both Inatsu et al. (2002) and Brayshaw et al. (2009), despite the large differences in heat capacity, surface friction, and moisture availability between oceans and continents.

The zonal structure in tropical and extratropical sea surface temperatures (SSTs), however, was found to be critical in shaping the stationary waves, albeit in very different ways. Tropical SST anomalies can influence stationary wave structure by modifying the regions of preferred upwelling in the Walker cell and associated divergent outflow (Inatsu et al. 2002; Brayshaw et al. 2009, among others) and thus act as a localized Rossby wave source. The thermal contrast between relatively warm wintertime oceans and cold wintertime continents in midlatitudes favors winter storm growth in the western part of ocean basins, and this enhancement is particularly strong for a southwest–northeast coastline orientation such as on the eastern coast of North America (Brayshaw et al. 2009, 2011). Western boundary currents can lead to locally enhanced diabatic heating and stronger transient eddies (Minobe et al. 2008; Smirnov et al. 2015; Wills et al. 2016; Parfitt et al. 2016) and thereby impact the stationary waves (Held et al. 2002; Kaspi and Schneider 2013). However, there is some ambiguity when imposing SSTs: Seager et al. (2002) conducted a set of experiments using an atmospheric general circulation model coupled to a mixed layer ocean to assess the impact of orography on the zonal asymmetries in the surface temperature distribution. Their results suggest that, if all mountains are removed, half of the surface temperature contrast between eastern North America and western Europe (and adjacent oceanic areas) would disappear, owing to a change in surface wind direction and resulting temperature advection. Furthermore, the stationary waves associated with land–sea contrast and SST zonal structure can interact nonlinearly with those associated with, for instance, the Tibetan Plateau and lead to a nonadditive total response (Held et al. 2002; Park et al. 2013), a theme we revisit in this paper.

The models used in these studies generally fall into two categories: first, aquaplanet models in which stationary

¹ However, deviations from this basic state on interannual time scales may be due to transient eddies (Held et al. 1989).

wave forcings are introduced in an idealized manner, but there is little attempt to reconstruct quantitatively the observed stationary wave field (e.g., Inatsu et al. 2002; Brayshaw et al. 2009, 2011; Saulière et al. 2012), or, second, comprehensive models in which a particular feature is omitted from a complete, “realistic” set of lower boundary conditions (e.g., Kitoh 1997; Broccoli and Manabe 1992; Wilson et al. 2009; Park et al. 2013; White et al. 2017). These comprehensive models, however, tend to be less flexible and tuned such that removing too many relevant forcings leads to unstable behavior. A model that can fully bridge these two categories is currently lacking, although we acknowledge the progress made by Brayshaw et al. (2009, 2011) and Saulière et al. (2012) in adding semirealistic boundary forcings to a nonlinear flat-bottomed GCM in a manner that allows for their removal.

While the aforementioned studies have made significant progress toward uncovering the building blocks of stationary waves, there are still several open questions that we address in this study:

- 1) Can one reconstruct the full magnitude of stationary waves by adding together the individual building blocks?
- 2) To what extent do the various building blocks of stationary waves interact nonlinearly with each other?
- 3) How does the degree of nonlinearity change between, for example, the Pacific sector and the Atlantic sector?
- 4) To the extent that nonlinearities exist, can we provide a diagnostic budget for the emergence of these nonlinearities?

The goal of this work is to attempt to answer these four questions. To achieve this goal, we have developed a simplified model that can represent stationary waves as faithfully as comprehensive general circulation models used for climate assessments, yet is still modular enough to allow one to build stationary waves by incrementally adding any or *all* relevant forcings (namely, land–sea contrast, ocean heat fluxes, and orography) to a zonally symmetric aquaplanet, or to remove them incrementally from a model configuration in which all of the forcings are initially present.

After introducing this novel model in section 2, we document the realism of its stationary waves in section 3. Section 4a demonstrates that in much of the Northern Hemisphere, the individual building blocks of stationary waves interact nonadditively, such that the sum of the responses to each building block does not equal the response when all are imposed simultaneously. The specific interactions among the forcings that lead to this nonadditive behavior are documented in section 4b, and

in section 4c we use the zonally anomalous steady-state thermodynamic balance to provide an explanation for this nonadditivity. Section 5 discusses which specific aspects of heat fluxes in the ocean (e.g., tropical warmpools and warmer extratropical SST near the western boundary) and of land–sea contrast (e.g., land–sea contrast in moisture availability, heat capacity, and surface friction) are most important for forcing stationary waves.

2. A model of an idealized moist atmosphere (MiMA), version 2

We construct an intermediate-complexity model that captures the important processes for stationary waves. While the ultimate goal is to understand nature, simpler models are valuable in order to isolate and subsequently synthesize fundamental physical processes, and serve as an important intermediate step between theory and comprehensive climate models. This approach has been espoused by Held (2005) and others as essential to narrowing the gap between the simulation and understanding of climate phenomena. Our goal is not to capture every detail of the observed stationary wave pattern, as even comprehensive general circulation models used in climate assessments do not succeed at this pursuit. Rather our goal is for the stationary waves in the intermediate model to be reasonably accurate—that is, to fall within the envelope of stationary waves simulated by CMIP5 models.

While it is possible to generate realistic stationary waves with a dry model of the atmosphere through an iterative process (Chang 2009; Wu and Reichler 2018), the physical connection to key forcings such as land–sea contrast in temperature and moisture is lost. Rather, we add three forcing mechanisms of stationary waves to a zonally symmetric moist aquaplanet model: orography, ocean horizontal heat fluxes, and land–sea contrast (i.e., the difference in heat capacity, surface friction, and moisture availability between oceans and continents).

We begin with the model of an idealized moist atmosphere (MiMA) introduced by Jucker and Gerber (2017). This model builds on the aquaplanet model of Frierson et al. (2006), Frierson et al. (2007), and Merlis et al. (2013). It includes moisture (and latent heat release), a mixed-layer ocean, Betts–Miller convection (Betts 1986; Betts and Miller 1986), and a boundary layer scheme based on Monin–Obukhov similarity theory. The Frierson et al. (2006) model uses a gray-radiation scheme and hence cannot resolve the interaction of shortwave radiation with ozone. It therefore lacks a realistic stratosphere. MiMA incorporates the Rapid Radiative Transfer Model (RRTM) radiation scheme

(Mlawer et al. 1997; Iacono et al. 2000). With this radiation scheme, we are able to incorporate the radiative impacts of ozone and water vapor into the model. This is in contrast to previous idealized studies of storm tracks and stationary eddies (e.g., Kaspi and Schneider 2013), and allows for the representation of a realistic stratosphere. Gravity waves have been added to the model following Alexander and Dunkerton (1999) and Cohen et al. (2013); this allows for the spontaneous generation of a quasi-biennial oscillation, and the details of the quasi-biennial oscillation in MiMA will be the subject of a future paper. The momentum associated with gravity waves that would leave the upper model domain is deposited in the levels above 0.85 hPa in order to conserve momentum and thereby avoid the complications noted by Shepherd and Shaw (2004) and Shaw and Shepherd (2007).

a. Land–sea contrast

Three different aspects of land–sea contrast are imposed: the difference in mechanical damping of near-surface winds between the comparatively rough land surface versus the smooth ocean, the difference in evaporation between land and ocean, and the difference in heat capacity. The roughness lengths for both moisture and momentum are varied between ocean and land to approximate land–sea contrasts. Over oceans, the roughness length for both momentum and moisture exchange is 3.21×10^{-5} m. Over land, the roughness length for momentum is increased by a factor of 5×10^3 , while the roughness length for moisture exchange is lowered by a factor of 1×10^{-12} . These factors were selected via trial and error in order to generate reasonable surface winds and evaporation for the most realistic experiment as compared to observational products as shown in the online supplemental material. The difference in roughness length between land and ocean for momentum is reasonable as compared to observations [Table 8 of Wiernga (1993)]. The magnitude of the reduction in the roughness length for moisture exchange over land that we impose is, on the face of it, unrealistic (Beljaars and Holtslag 1991). However, the resulting difference in the drag coefficient between land and ocean used by Monin–Obukhov similarity theory is approximately a factor of 4.5 for momentum and 0.75 for moisture, and it is the drag coefficients that actually affect the large-scale flow. If anything, the resulting reduction in moisture availability over land is not strong enough, and precipitation and evaporation biases are still present over desert regions (see Fig. S9 in the online supplemental material).

The heat capacity for oceanic grid points is set to $4 \times 10^8 \text{ J K}^{-1} \text{ m}^{-2}$ (equivalent to a mixed layer depth of

100 m) and for land grid points to $8 \times 10^6 \text{ J K}^{-1} \text{ m}^{-2}$ (equivalent to a mixed layer depth of 2 m). An oceanic mixed layer depth of 100 m leads to a $\sim 1\text{--}2$ -month delay in the seasonal cycle of oceanic temperatures as compared to observations, but helps ensure reasonable values of surface temperature near the poles (Jucker 2019). For experiments with no land–sea contrast, the oceanic mixed layer depth and roughness is used everywhere. We use a high-resolution land mask to determine land versus ocean; thus, the surface is accurately represented on the latitude versus longitude grid on which, for example, surface fluxes are computed.

For experiments with land–sea contrast, we set the surface albedo as

$$\text{albedo} = 0.27 + \frac{0.75 - 0.27}{2} \left[1 + \tanh\left(\frac{\phi - 75^\circ}{5^\circ}\right) \right] + \frac{0.75 - 0.27}{2} \left[1 - \tanh\left(\frac{\phi + 70^\circ}{5^\circ}\right) \right], \quad (1)$$

where ϕ is latitude, which leads to higher albedo values over the Arctic and Antarctic that smoothly transition to 0.27 in the midlatitudes and tropics. MiMA has no clouds, and an albedo of 0.27 was primarily tuned to approximate the shortwave effects of clouds. For experiments with no land–sea contrast the albedo is set to 0.27 everywhere. The increase in polar surface albedo in experiments with land–sea contrast leads to globally averaged surface temperature cooling by ~ 1.7 K.

b. Zonal asymmetries in the ocean

Ocean horizontal heat transport (often referred to as Q fluxes; e.g., Merlis et al. 2013) is specified in order to force zonal asymmetries in surface temperatures following Jucker and Gerber (2017) so that the western part of oceanic basins are warmer than the eastern part. These Q fluxes are necessary as we do not have a dynamical ocean, although we acknowledge that ocean heat transport is affected by the atmospheric stationary wave structure. Merlis et al. (2013) and Jucker and Gerber (2017) specified a zonally uniform ocean horizontal heat transport as

$$\nabla \cdot \mathbf{F}_o(\phi) = Q_o \frac{1}{\cos \phi} \left(1 - \frac{2\phi^2}{\phi_o^2} \right) \exp\left(-\frac{\phi^2}{\phi_o^2}\right), \quad (2)$$

with $Q_o = 30 \text{ W m}^{-2}$ and $\phi_o = 16^\circ$ [repeated from Eq. (2) of Jucker and Gerber (2017); see also Merlis et al. (2013)]. All experiments here employ this meridional heat flux although we set $Q_o = 26 \text{ W m}^{-2}$.

Jucker and Gerber (2017) explored zonal heat transport by the ocean, and added an idealized warm pool.

Here we implement a warm pool and an approximation of western boundary currents. The net effect of the formulas described below is shown in Fig. S1. We do not aim to specifically capture the small-scale features

present in observations, but rather the large-scale zonal transport of heat with the goal of capturing stationary waves as realistically as CMIP5 models. The chosen representation of the Pacific warm pool is

$$\nabla \cdot \mathbf{F}_{\text{Pac}}(\phi, \lambda) = \begin{cases} \left[1 - \left(\frac{\phi}{35^\circ} \right)^4 \right] Q_{\text{Pacific}} \cos[5/3(\lambda - 150^\circ)], & 96^\circ \leq \lambda \leq 312^\circ \quad \text{and} \quad |\phi| < 35^\circ \\ 0, & \text{otherwise} \end{cases}. \quad (3)$$

An Atlantic “warm pool” is added analogously:

$$\nabla \cdot \mathbf{F}_{\text{Atl}}(\phi, \lambda) = \begin{cases} \left[1 - \left(\frac{\phi}{35^\circ} \right)^4 \right] Q_{\text{Atlantic}} \cos[4(\lambda - 310^\circ)], & 288^\circ \leq \lambda \leq 18^\circ \quad \text{and} \quad |\phi| < 35^\circ \\ 0, & \text{otherwise} \end{cases}. \quad (4)$$

Note that both the Atlantic and Pacific warm pool anomalies add no net heat to the atmosphere, and merely redistribute heat zonally within the tropics. For experiments in which a warm pool is included, $Q_{\text{Pacific}} = 18 \text{ W m}^{-2}$ and $Q_{\text{Atlantic}} = 15 \text{ W m}^{-2}$. These values are chosen in order to capture the observed zonal asymmetry in sea surface temperature (Figs. S1 and S8).

To approximate western boundary currents and the subtropical and extratropical ocean gyres, we redistribute heat in the extratropics as well. The goal is to capture zonal asymmetry on large scales in SSTs, not to accurately capture the fine structure of meridional heat transport by the western boundary currents. The chosen representation of the Gulf Stream and Kuroshio is as follows:

$$\nabla \cdot \mathbf{F}_{\text{Gulf}}(\phi, \lambda) = Q_{\text{Gulf}} \left\{ \left[1 - \left(\frac{\phi - 37^\circ}{10^\circ} \right)^4 \right] (A + B) + 0.7 \left[1 - \left(\frac{\phi - 67^\circ}{10^\circ} \right)^4 \right] (C + D) \right\}, \quad (5)$$

where

$$A = \cos[4(\lambda - 290.5^\circ)], \quad 268^\circ \leq \lambda \leq 358^\circ \quad \text{and} \\ 27^\circ < \phi < 47^\circ, \quad (6)$$

$$B = 0.535 \sin[8(\lambda - 290.5^\circ)], \quad 268^\circ \leq \lambda \leq 313^\circ \quad \text{and} \\ 27^\circ < \phi < 47^\circ, \quad (7)$$

$$C = \cos[3(\lambda - 348^\circ)], \quad 258^\circ \leq \lambda \leq 18^\circ \quad \text{and} \\ 57^\circ < \phi < 77^\circ, \quad (8)$$

$$D = 0.25 \cos[6(\lambda - 288^\circ)], \quad 243^\circ \leq \lambda \leq 303^\circ \quad \text{and} \\ 57^\circ < \phi < 77^\circ, \quad \text{and} \quad (9)$$

$$\nabla \cdot \mathbf{F}_{\text{Kuroshio}}(\phi, \lambda) = Q_{\text{Kuroshio}} \left[1 - \left(\frac{\phi - 37^\circ}{10^\circ} \right)^2 \right] (E + F), \quad (10)$$

where

$$E = \cos[4(\lambda - 155^\circ)], \quad 132.5^\circ \leq \lambda \leq 222.5^\circ \quad \text{and} \\ 27^\circ < \phi < 47^\circ, \quad \text{and} \quad (11)$$

$$F = -0.65 \cos[6(\lambda - 165^\circ)], \quad 180^\circ \leq \lambda \leq 240^\circ \quad \text{and} \\ 27^\circ < \phi < 47^\circ. \quad (12)$$

Terms A, B, \dots, F are zero outside of the regions indicated.

Similar to the imposed warm pools, the Kuroshio and Gulf Stream anomalies add no net heat to the atmosphere, and just flux heat from the eastern or central part of oceanic basins to the western part. Hence the globally averaged temperature is essentially unchanged, and complications that arise from differences in globally averaged temperature (Thomson and Vallis 2018) are not relevant here. The poleward component of the Gulf Stream forcing (terms C and D) warms the Norwegian Sea and cools the Labrador Sea and adjacent areas in northern Canada. For experiments in which western boundary oceanic heating is included, $Q_{\text{Gulf}} = 60 \text{ W m}^{-2}$ and $Q_{\text{Kuroshio}} = 25 \text{ W m}^{-2}$. Our representation of the Gulf Stream and Kuroshio is not intended to represent the small-scale ocean frontal features, but rather to

force a broad region of heating. It is conceivable that imposing more realistic small-scale frontal features in a high-resolution model would lead to a different stationary wave response.

The idea behind the parameters chosen in Eqs. (3)–(12) is to smoothly connect a moist aquaplanet with no Q fluxes or with Q fluxes that only flux heat from the deep tropics to the subtropics (Merlis et al. 2013; Jucker and Gerber 2017) to a configuration that, in a gross sense, mimics observed Q fluxes. Hence, we specify analytic functions in latitude and longitude that resemble on large scales those observed, but with tunable magnitude such that these features can be turned off. The net effect of these Q fluxes is shown in Fig. S1, which compares favorably on large scales to observed Q fluxes [Fig. 1 of Forget and Ferreira (2019) or Fig. 2 of Trenberth et al. (2019)]. We are currently working on a more realistic prescription of the Q fluxes on small scales, and this work will be reported in a future study focusing on the impacts of a narrower Gulf Stream, Agulhas Current, and Kuroshio.

No representations of Southern Hemisphere oceanic heat fluxes, and specifically of the fluxes that help drive the South Pacific convergence zone, have been included. Therefore, in this paper we focus on the Northern Hemisphere only, although our integration with all forcings captures Southern Hemisphere stationary waves in a qualitative sense too.

c. Topography and additional details of the model forcing

Observed topography is used for the most realistic experiment, albeit at the resolution of the model with no effort to adjust the amplitude to preserve ridge heights (sometimes referred to as envelope topography), but with regularization included as in Lindberg and Broccoli (1996) to minimize Gibbs ripples. For experiments without topography, the topographic height over land areas is set uniformly to 15 m. For code implementation reasons we do not use zero, but 15 m is sufficient to suppress Rossby waves generated by topography. For simplicity we refer to all mountains in central Asia as the Tibetan Plateau, although we acknowledge that mountains farther north near Mongolia may be more important for forcing stationary waves (White et al. 2017).

CO_2 is a scalar constant, set to 390 ppm throughout the atmosphere to roughly approximate concentrations during the period of the observational and reanalysis data we use to assess the model. In the simulations presented here, ozone is specified as the time and zonal mean of annual-mean ozone specified for the CMIP5 forcing from 1850 through 1880 (Cionni et al. 2011); the

TABLE 1. MiMA experiments, with “Y” indicating a forcing is on and “N” indicating a forcing is off. The isolated nonlinear response to topography can be deduced from experiment 1, while the full nonlinear response is the difference between experiments 7 and 6. The isolated nonlinear response to land-sea contrast can be deduced from experiment 2, while the full nonlinear response is the difference between experiments 7 and 4. The isolated nonlinear response to ocean heat fluxes can be deduced from experiment 3, while the full nonlinear response is the difference between experiments 7 and 5.

Expt	Orography	Land-sea contrast	Ocean heat fluxes
0	N	N	N
1	Y	N	N
2	N	Y	N
3	N	N	Y
4	Y	N	Y
5	Y	Y	N
6	N	Y	Y
7 (ALL)	Y	Y	Y

ozone varies in latitude and pressure but not in longitude or time. Specifying contemporary ozone concentrations leads to a slightly lower stratospheric sudden warming frequency and a stronger stratospheric vortex.

The simulations include a seasonal cycle, with the year length set as 360 days and each “month” as 30 days long. The obliquity is set as 23.439° , and Earth’s orbit is fixed as a circle at 1 AU. The spring equinox is on day 90 of the year ($0.25 \times 360 = 90$), that is, 30 March.

d. Experiments

Table 1 lists the seven experiments included in this paper, each experiment lasting 38 years after discarding at least 10 years of spinup. In addition to these seven experiments, **section 5** describes sensitivity experiments that explore the region in which ocean heat fluxes are most important for stationary waves. **Section 5** also describes sensitivity experiments that assess the relative importance of three different elements of land-sea contrast: the difference in mechanical damping of near-surface winds between the land and ocean, the difference in evaporation between land and ocean, and the difference in heat capacity. All integrations here were run at a horizontal resolution of triangular truncation 42 (T42), although the most realistic configuration was also run at T85 with similar results. All integrations were run with 40 vertical levels with a model lid near 70 km. The stationary waves are compared to those present from 1985 to 2004 in the historical integrations from 42 CMIP5 models, and results are similar if we use the 2009–29 period in the RCP8.5 integrations (not shown).

To emphasize differences from previous idealized modeling studies, we note that this model does not use a

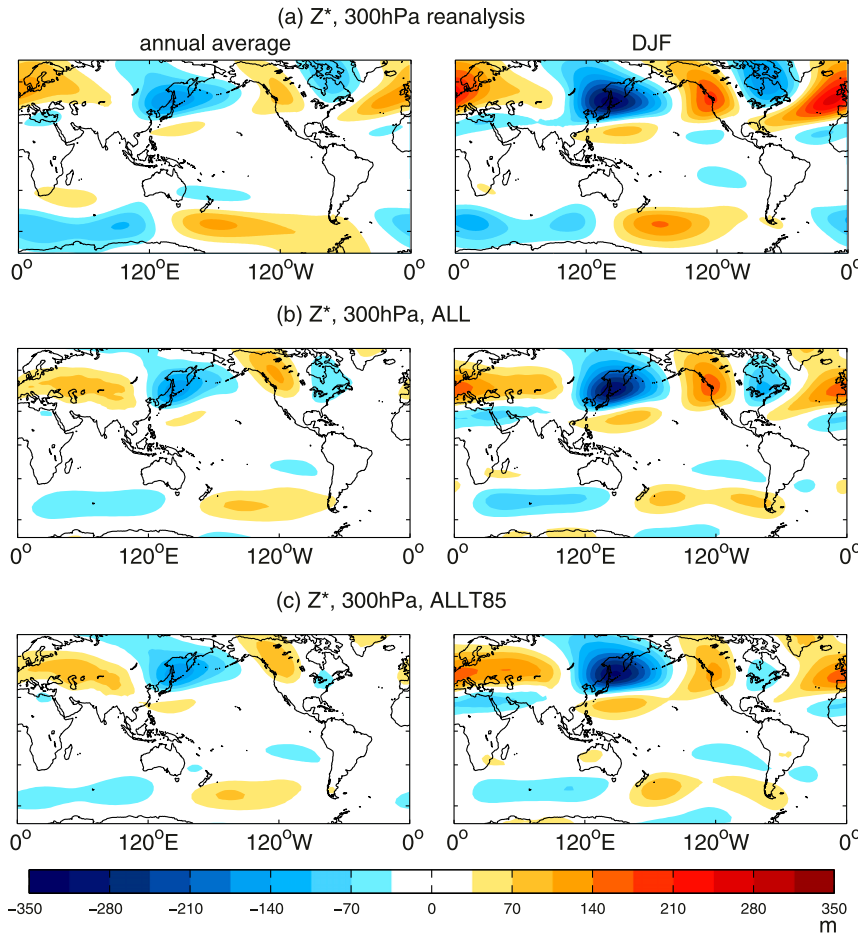


FIG. 1. Geopotential height at 300 hPa (m) in the annual average and in December–February in (a) ERA5, (b) ALL, the most realistic integration (integration 7 on Table 1), and (c) the T85 ALL integration. The contour interval is 35 m.

Downloaded from <http://journals.ametsoc.org/jul/article-pdf/31/13/5611/4955256/pdf190181.pdf> by guest on 20 July 2020

stratospheric sponge layer, Rayleigh damping, or temperature relaxation of any kind. All damping on large scales is done by physically motivated processes (e.g., a gravity wave scheme for the middle atmosphere and Monin–Obukhov similarity theory for the surface layer), as in comprehensive general circulation models. Furthermore, we do not impose diabatic heating, but rather parameterize the underlying processes that influence diabatic heating. The surface temperature is not prescribed. Rather, it changes in response to changing surface fluxes of sensible heat, latent heat, and radiation. The novelty yet flexibility of this model allows us to dissect the building blocks of stationary waves and their nonlinear interactions more cleanly than has been done before.

The code will be made publicly available in MiMA release v2.0. The exact technical details and extensive parameter descriptions of MiMA release v1.0.1 can be found in the online documentation at <https://mjucker.github.io/MiMA>, and the key changes in

MiMA relative to the model of [Jucker and Gerber \(2017\)](#) are documented above.

3. Stationary waves in MiMA with all forcings

We now assess the fidelity of the stationary waves in the most realistic configuration of MiMA, which includes all relevant forcings (hereafter ALL; experiment 7 in Table 1). We begin with the stationary wave field in 300-hPa geopotential height in ERA5 ([Copernicus Climate Change Service 2017](#); [Hersbach and Dee 2016](#); Fig. 1a) and ALL (Fig. 1b), defined here as the deviation of the time-averaged height field from its zonal mean. In both the model and in observations, lower heights are present over East Asia and the west Pacific and also over the eastern United States, while higher heights are present over western North America and western Eurasia. The correspondence is similarly close at 850 hPa (Fig. S2) and 50 hPa (Fig. S3).

There are differences in the strength of the stationary waves between MiMA and observations (e.g., over the North Atlantic and North America), but we now show that stationary waves in MiMA are just as good as those in comprehensive general circulation models. The relative magnitude of 300-hPa geopotential height stationary waves at 50°N averaged from December through February is quantified in Fig. 2a for ERA5 (green), ALL (blue; integration 7 in Table 1), and 42 different CMIP5 models (thin lines). We focus on 50°N as it is near where stationary wave amplitude peaks, although results are similar at, say, 45° or 55°N (not shown). The biases in ALL are not any worse than those in many CMIP5 models, and MiMA lies well within the envelope of the CMIP5 models for nearly all longitudes.

Figure 3a is the same as Fig. 2a, but for the stationary waves at 50 hPa. The stratospheric stationary waves in MiMA are nearly identical to those in reanalysis data, and markedly better than in most CMIP5 models. During wintertime, stationary eddies couple with the stratosphere (Wang and Kushner 2011), which has been shown to affect the north–south position of the Atlantic storm track (Shaw et al. 2014). The stratospheric sudden warming frequency in ALL is 0.38 events per year, and in experiment 5 (no east–west q fluxes, but with land–sea contrast and topography) the frequency is 0.30 events per year. In all other experiments SSW frequency is below 0.03 events per year. It is possible that the enhanced frequency of occurrence of sudden warmings in ALL modulates the tropospheric stationary waves, but quantifying this effect is left for possible future work.

To address the sampling uncertainty in the stationary waves, we compute separate averages for the first 19 and last 19 years of the 38-yr-long ALL integration, and show the stationary waves in orange lines on Fig. 2b. The blue ALL line is repeated from Fig. 2a. For most of the NH the blue line is not visible because of the close correspondence with the two orange lines.

The results are also not sensitive to the horizontal resolution. Figure 1c shows the stationary wave pattern in an experiment performed at T85 resolution, and the stationary waves are quantitatively similar. The black line in Fig. 2b shows the 50°N stationary waves for the T85 ALL integration, and it is very close to the corresponding lines for T42 resolution, although somewhat worse over North America. Therefore, for the remainder of this manuscript we focus on integrations performed at T42 resolution.

A complementary perspective on the fidelity of the stationary waves in ALL can be reached from the wind field, and we include a comparison of observed and

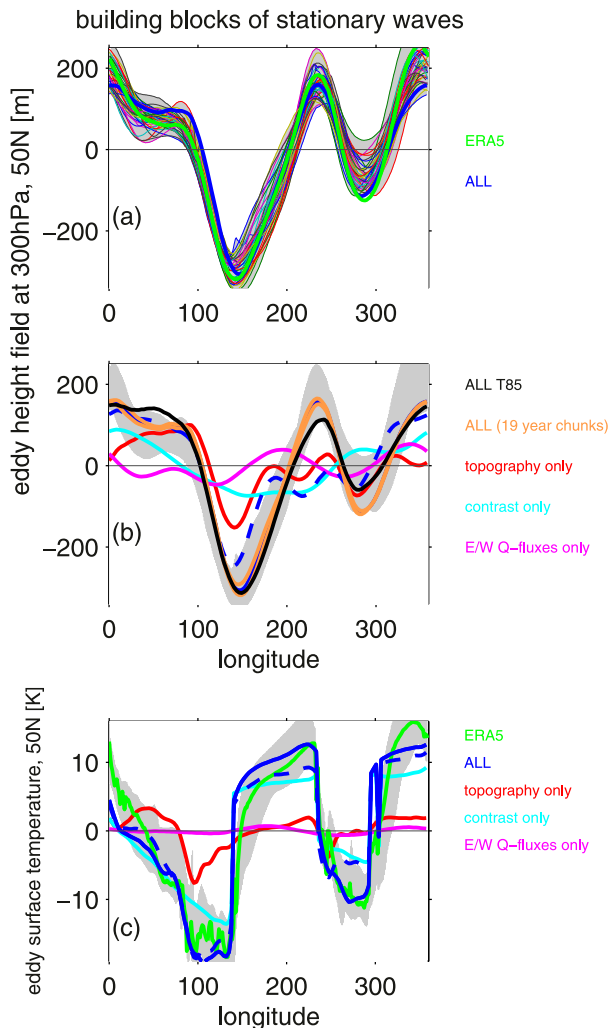


FIG. 2. Deviation of 300-hPa geopotential height at 50°N from the zonal average from December through February in (a) ERA5 (green), the most realistic MiMA integration in which all forcings are included (blue), 42 different CMIP5 models (thin lines), and the maximum and minimum for the 42 CMIP5 models (gray). (b) As in (a), but for the first 19 and second 19 years of ALL (orange), ALL performed at T85 resolution (black), integrations with topography only (red), land–sea contrast only (cyan), and ocean heat fluxes only (magenta), and for the sum of these three integrations (dashed blue). The stationary waves in MiMA are compared to those present from 1985 to 2004 in the historical integrations from 42 CMIP5 models. (c) As in (b), but for surface temperature at 50°N.

modeled winds at 300 and 850 hPa in Figs. S4 and S5. Figure S6 shows that the stationary waves are similar in January through March. The climatological tropical diabatic heating in ALL is shown in Fig. S7, and it compares favorably to that in reanalysis products [Fig. 3 of Wright and Fueglistaler (2013)]. The climatological surface temperature and evaporation in ALL and in reanalysis data are shown in Figs. S8 and S9. Briefly,

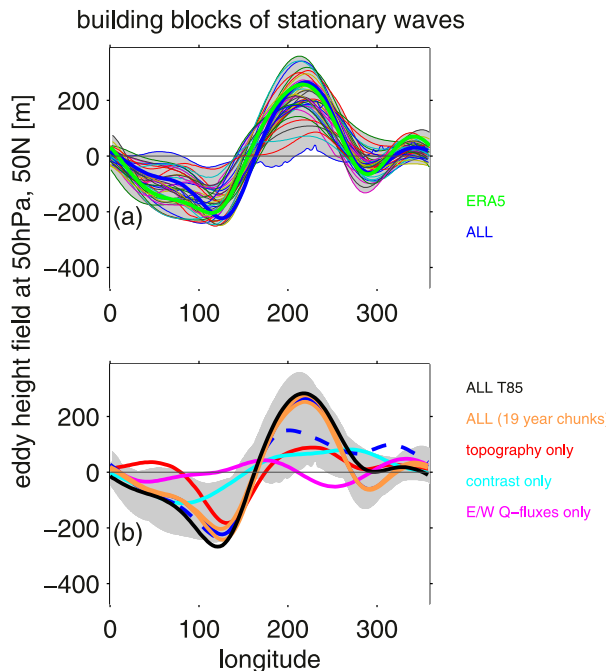


FIG. 3. As in Figs. 2a and 2b, but for 50 hPa.

ALL captures the observed large-scale features reasonably well for all of these diagnostics, and a complete discussion can be found in the supplemental material.

4. The (non)linearity of the stationary wave building blocks

We now use MiMA to probe the building blocks of stationary waves. We address each of the questions posed in the introduction separately.

a. Do the stationary waves in ALL equal the sum of the stationary wave response to each forcing?

We first consider whether the stationary wave pattern can be decomposed linearly into the various forcings. Figure 4a repeats the stationary wave pattern for ALL from Fig. 1b, and Fig. 4b shows the sum of the stationary wave patterns in the topography only (experiment 1), land-sea contrast only (experiment 2), and ocean heat flux only experiments (experiment 3; i.e., the stationary waves are calculated for each integration separately and then summed). While the stationary wave field over Europe in ALL appears to be associated with the linear summation of the forcings, the stationary wave field over the Pacific is not. First, the low over East Asia and the west Pacific is approximately 30% stronger in ALL than when the individual forcings are summed. Even larger discrepancies are evident over the northeast Pacific and western North America: there is no ridge when each

forcing is imposed in isolation, while ALL simulates a ridge in this region as observed [Fig. 1a; similar to Ting et al. (2001), although they imposed diabatic heating and not the underlying forcings that drive stationary waves]. Finally, the ridge over western Siberia is stronger when each forcing is imposed in isolation than in ALL. Overall, the stationary waves in ALL do not resemble a simple linear summation of the individual response to each forcing over much of the Northern Hemisphere.

The nonadditive behavior is summarized in Fig. 2b. The orange curves in Fig. 2b repeat the stationary wave pattern in ALL for geopotential height at 300 hPa and 50°N, and the gray shading repeats the spread in the 42 CMIP5 models. Figure 2b adds on experiments with topography only (red), ocean heat fluxes only (magenta), and land-sea contrast only (cyan), and the dotted blue line in Fig. 2b is the sum of the stationary waves for these three individual forcing experiments. In the Pacific and North American sectors from 150° through 250°E, the summed response to the individual forcings is weaker than the response when all forcings are imposed together (substantial nonlinearities in this region have been noted before; e.g., Nigam et al. 1988; Held et al. 2002). In the Euro-Atlantic sector from 330° through 100°E, however, linearity is a reasonable assumption. Over the Atlantic and European sectors land-sea contrast plays the largest role, and topography plays a larger role farther to the east over western Russia. Orography is the most important factor for the Pacific sector, although land-sea contrast has a nonnegligible role. Note, however, that one must be cautious in ranking the relative importance of the factors if the forcings interact nonlinearly as they do in the Pacific sector.

Figure 3b is similar to Fig. 2b but for the stationary waves at 50 hPa. No single forcing dominates the forcing of stratospheric stationary waves, although orography (red) is seemingly most important [largely consistent with Inatsu et al. (2002)] in the Pacific and land-sea contrast above Eurasia. The sum of the stratospheric responses to each individual forcing is quantitatively similar to the response in ALL in the Eastern Hemisphere, although not in the Western Hemisphere where the magnitude is weaker in the North American sector and stronger over the Atlantic.

Similar nonadditive behavior is also evident in the wavenumber composition of the stationary waves in both the troposphere and stratosphere. Figure 5 shows the wavenumber decomposition of the stationary wave field in ERA5, ALL, and the sum of the responses for the topography only, land-sea contrast only, and ocean heat fluxes only integrations. Wavenumber 1 is somewhat too weak in ALL as compared to reanalysis due to the relative weakness of the North Atlantic ridge

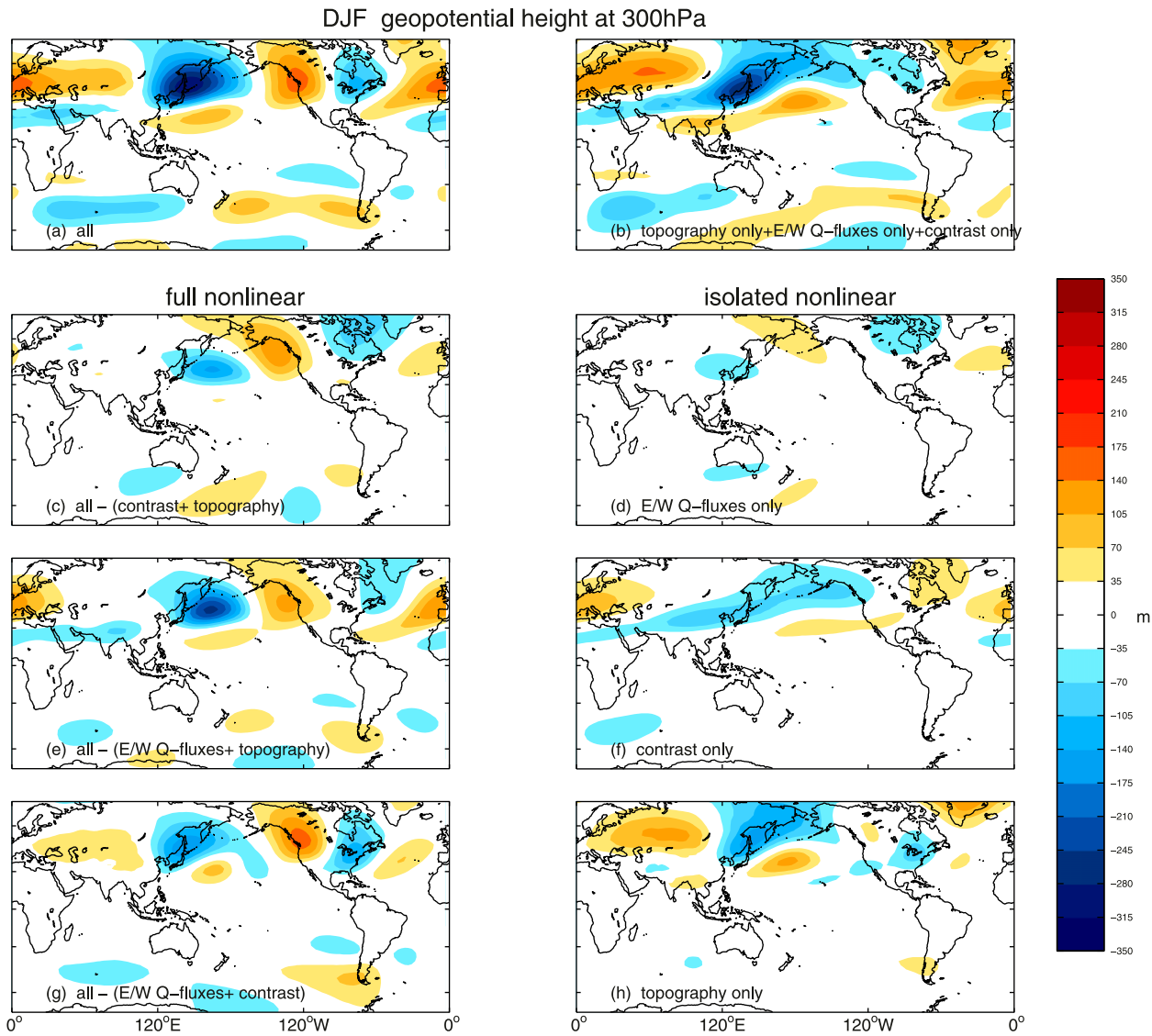


FIG. 4. (a) Deviation of December–February 300-hPa geopotential height from the zonal average in ALL (repeated from Fig. 1b). (b) As in (a), but for the sum of integrations with topography only, land–sea contrast only, and ocean heat fluxes only. (c) The difference between ALL and the integration with land–sea contrast and topography. (d) The integration with only ocean heat fluxes. (e) The difference between ALL and the integration with ocean heat fluxes and topography. (f) The integration with only land–sea contrast. (g) The difference between ALL and the integration with ocean heat fluxes and land–sea contrast. (h) The integration with only topography. The contour interval is 35 m.

Downloaded from <http://journals.ametsoc.org/jcli/article-pdf/33/13/5611/4955256/jcli190181.pdf> by guest on 20 July 2020

[cf. Fig. 2 of Garfinkel et al. (2010)], and this bias is present in the sum of the responses to each forcing as well. In contrast, wavenumber 2 in ALL is reasonable, but too weak by nearly 50% in the sum of the responses to each forcing. This weakening of wavenumber 2 is consistent with the lack of a northwest North America ridge in Fig. 4b [cf. Fig. 2 of Garfinkel et al. (2010)].

Zonal asymmetries in surface temperatures are also nonadditive in response to each of the three forcings. Figure 2c shows the zonal asymmetries in surface temperatures in ALL (blue), in ERA5 (green), and for

42 CMIP5 models (gray shading). The surface temperatures in ALL follow those in ERA5 at nearly all longitudes, and are nearly as reasonable as those in CMIP5 models. Figure 2c also contains the zonal asymmetries in surface temperature for the topography only, ocean heat fluxes only, and land–sea contrast only experiments, and the dotted blue line in Fig. 2c is the sum of the zonally asymmetric component of surface temperature for these three individual forcing experiments. Over the eastern Atlantic and western Europe, surface temperatures are up to 1.7 K warmer in ALL than in the linear sum of the

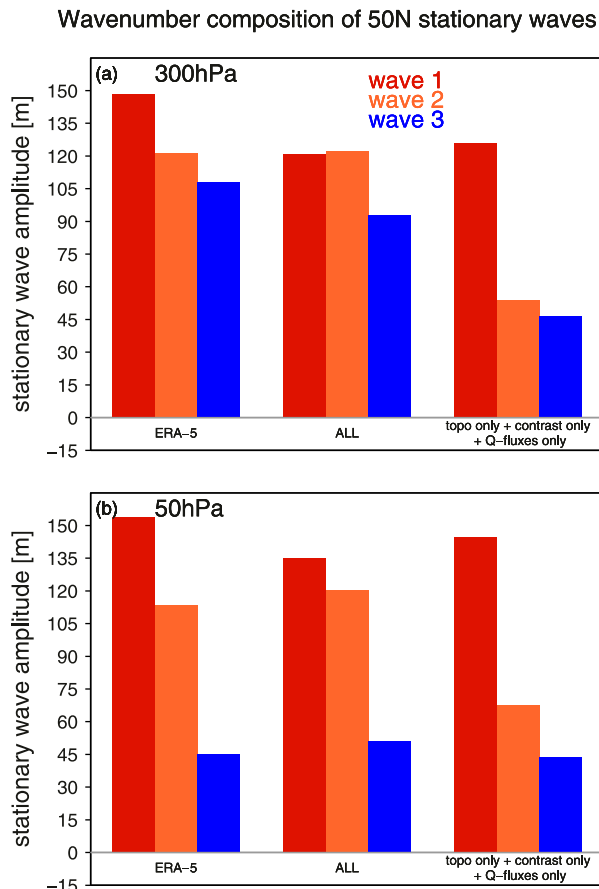


FIG. 5. Zonal wavenumber decomposition of the stationary waves at 50°N for ERA5, ALL, and the sum of integrations with topography only, land-sea contrast only, and ocean heat fluxes only, at (a) 300 and (b) 50 hPa.

response to each forcing. In this region land-sea contrast (cyan) is the dominant forcing due to the thermal inertia of the Atlantic Ocean from summer to winter, although topography contributes up to ~ 1.8 K of warming in this region. Eastern Canada is 3.5 K colder in ALL than in the simple linear summation of the response to ocean heat fluxes only, land-sea contrast only, and topography only, and results are similar at 40°N over the eastern United States (not shown). While land-sea contrast is the strongest individual forcing in this region, the substantial difference between ALL and the sum of the individual responses highlights that surface temperatures respond nonadditively to the three forcings. These results support those of Brayshaw et al. (2009) and Seager et al. (2002), who highlight the importance of the Rocky Mountains in generating stationary waves that enhance the temperature difference between the eastern and western margins of the North Atlantic. This nonadditive surface temperature response has implications for studies that impose SSTs

in (for example) general circulation models and then proceed to study the forcings leading to stationary waves: such a procedure underestimate the degree of nonlinearity present.

b. Which forcings interact nonadditively?

We now explore why the stationary wave pattern in ALL differs from the summation of the response to each forcing applied individually. Specifically, which forcings are most responsible for the nonadditive behavior evident in section 4a? Before proceeding we review the definition of the isolated and full nonlinear response of Held et al. (2002). The response to some source of asymmetry A in MiMA can be denoted as $M(A)$. Let F represent all three forcings in the most realistic configuration such that the response to F is $M(F)$. As in Held et al. (2002), we refer to $M(A)$ as the isolated nonlinear response to A and $M(F) - M(F - A)$ as the full nonlinear response to A . If we consider adding the three different parts of the forcing in sequence, the isolated nonlinear response to A occurs when A is added first, while the full nonlinear response to A occurs when A is added last (or is the first to be removed).

The bottom three rows of Fig. 4 show the 300-hPa stationary wave response in geopotential height to each forcing imposed in isolation (right column; *isolated nonlinear response*) and also when each forcing is removed from ALL (left column; the *full nonlinear response*), and similar figures but for streamfunction at 300 and 850 hPa are included in Figs. S10 and S11. For example, Fig. 4c considers the difference in stationary waves between ALL and the experiment where both land-sea contrast and topography are imposed but ocean heat flux zonal asymmetry is not. Hence, the stationary wave pattern in Fig. 4c is that forced by ocean heat flux zonal asymmetries when imposed on a basic state that already includes land-sea contrast and topography (the full nonlinear response). This pattern in Fig. 4c can be compared to the isolated nonlinear response to ocean heat flux zonal asymmetries in Fig. 4d. Ocean heat flux zonal asymmetries in isolation have a limited impact on the Pacific sector stationary wave pattern, but when imposed on the basic state set up by topography and land-sea contrast the effect more than doubles in strength [consistent with Blackmon et al. (1987), among others]. Note that zonal asymmetries in ocean heat fluxes have a minimal effect on European stationary waves. Section 4c will provide a diagnostic accounting for this difference between the isolated nonlinear and full nonlinear responses.

Figure 4e shows the impact that land-sea contrast has on stationary waves when imposed on a basic state that already includes topography and east-west zonal asymmetries, while Fig. 4f shows the isolated nonlinear

TABLE 2. Summary of nonlinearities.

Region	Forcing		
	Ocean heat fluxes	Land-sea contrast	Topography
Northwest Pacific	Isolated nonlinear response weaker	Isolated nonlinear response weaker	Linear
Western North America	Ridge only in full nonlinear	Opposite-signed responses	Ridge only in full nonlinear
Western Atlantic	Not important	Opposite-signed responses	Isolated nonlinear response weaker
European sector	Isolated nonlinear response weaker	Isolated nonlinear response weaker	Not important
Central Eurasia	Not important	Not important	Isolated nonlinear response stronger

response. Over Europe the full nonlinear and isolated nonlinear responses are similar, although the full nonlinear response is stronger. In contrast, over the Pacific sector they differ qualitatively, with only the full nonlinear response indicating a trough over the west Pacific, a ridge over the west coast of North America, and a trough over northeastern Canada.

Finally, Fig. 4g shows the full nonlinear response to topography, while Fig. 4h shows the isolated nonlinear response to topography. Over Eurasia the full nonlinear response is weaker than the isolated nonlinear response. In contrast, the full nonlinear response over western North America (to the Rockies) is stronger than the isolated

nonlinear response. Only over the northwest Pacific are the isolated nonlinear and full nonlinear responses similar.

In summary, there are four key differences between the isolated nonlinear and full nonlinear responses: 1) land-sea contrast and 2) ocean heat flux asymmetries have a weaker impact on the northwest Pacific low in isolation as compared to the full nonlinear response, and 3) the response to the Rockies is weaker in isolation as compared to the full nonlinear response, whereas 4) the response upstream of the Tibetan Plateau is stronger in isolation as compared to the full nonlinear response. These four nonlinearities, as well as additional weaker instances, are summarized in Table 2. These nonlinearities

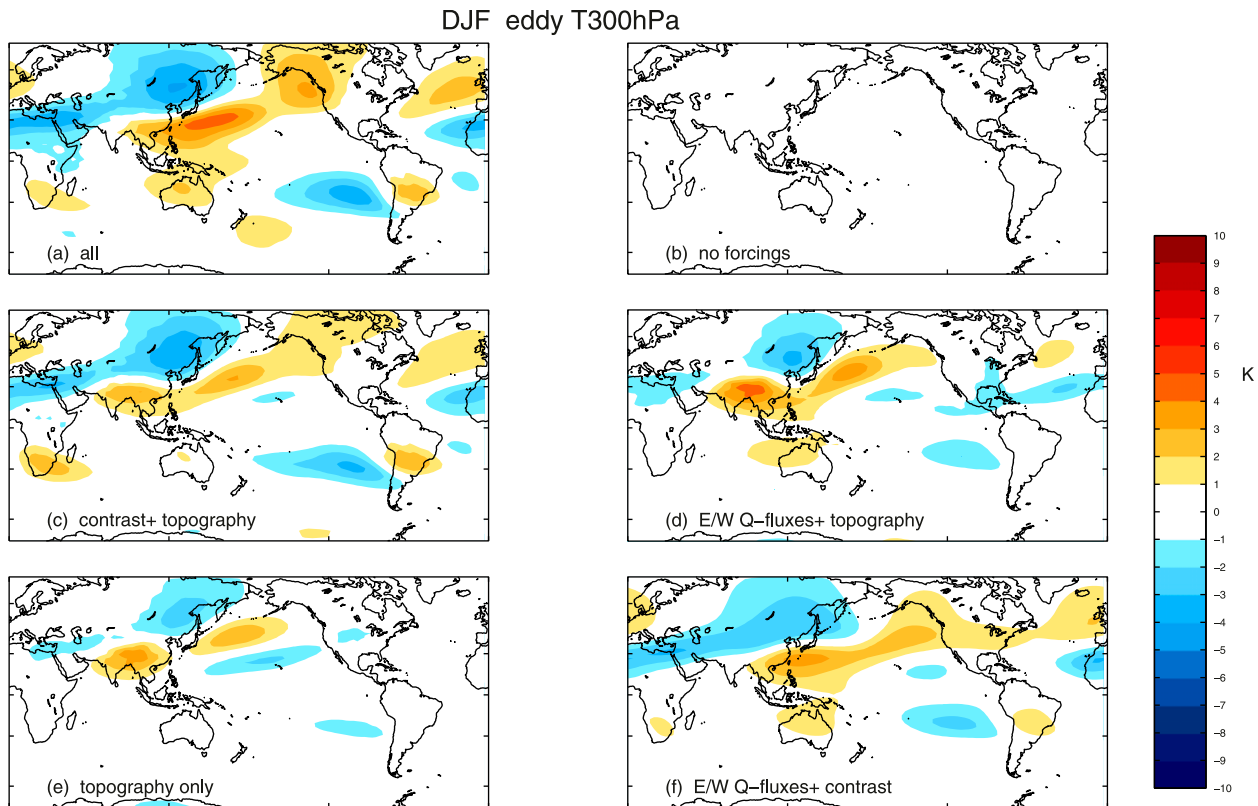


FIG. 6. The zonally asymmetric component of the 300-hPa temperature field \bar{T}^* (with the bar indicating a time average) that is acted upon by the various forcings in (a) ALL, (b) a configuration with no zonally asymmetric forcings, (c) an integration with both land-sea contrast and topography, (d) an integration with both ocean heat fluxes and topography, (e) an integration with topography only, and (f) an integration with both land-sea contrast and ocean heat fluxes. Tendencies plotted here and in subsequent figures are shown as temperature tendencies rather than potential temperature tendencies.

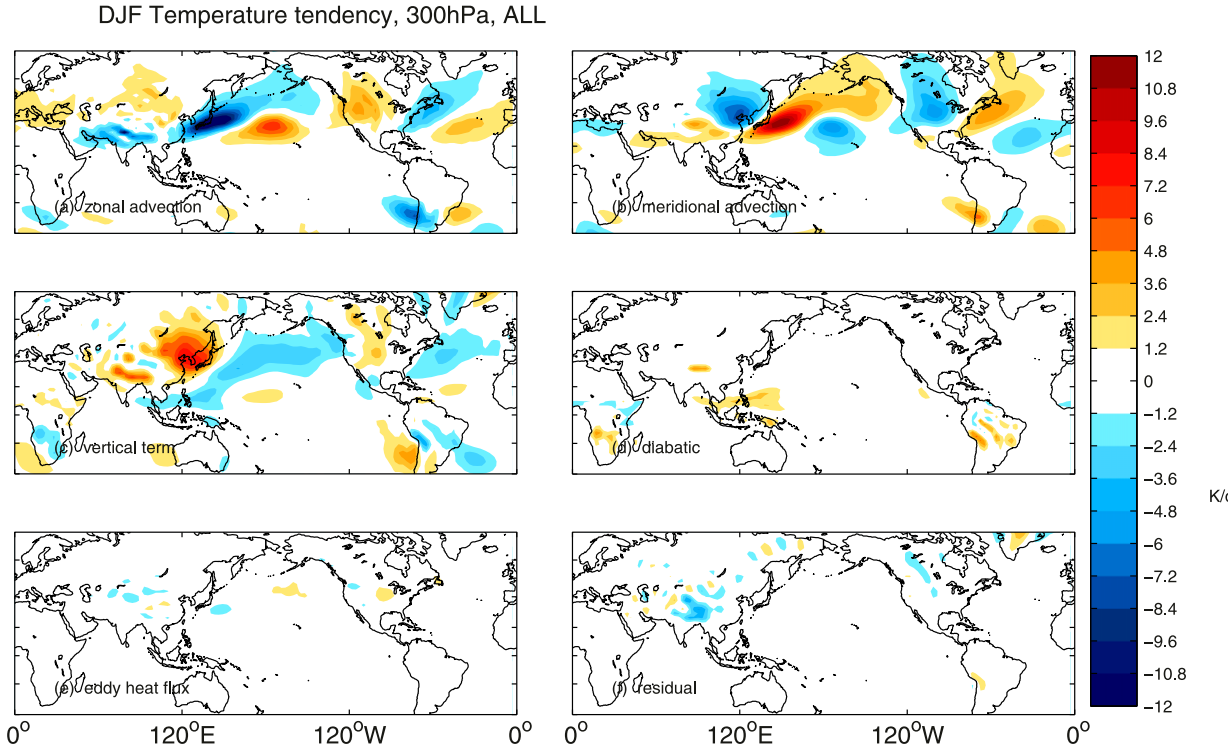


FIG. 7. Zonally asymmetric steady-state thermodynamic balance for ALL at 300 hPa following Wills and Schneider (2018): (a) zonal advection term $[-\bar{u}(\partial\bar{\theta}/\partial x)]^*$; (b) meridional advection term $[-\bar{v}(\partial\bar{\theta}/\partial y)]^*$; (c) vertical term $[-\bar{\omega}(\partial\bar{\theta}/\partial p)]^*$; (d) diabatic heating term (\bar{Q}^*); (e) transient eddy heat flux term $[-\nabla \cdot (\bar{\mathbf{v}}'\bar{\theta}')^*]$; (f) residual of the budget. The contour interval is 1.2 K day^{-1} .

are similar if we focus on streamfunction (see Figs. S10 and S11).

c. Why do the isolated nonlinear and full nonlinear responses differ?

The goal of this subsection is to explain why the isolated nonlinear and full nonlinear responses differ. First, we introduce the zonally anomalous steady-state thermodynamic balance, our main tool for explaining these differences. We then evaluate all terms in the budget for ALL in order to establish context. Next, we utilize the budget to explain the differences between the full nonlinear and isolated nonlinear responses. Finally, we consider whether other budgets provide additional insight into the difference between the isolated nonlinear and full nonlinear responses.

The zonally anomalous steady-state thermodynamic balance can be written as [Eq. (11) of Wills and Schneider (2018)]

$$\left(\bar{u} \frac{\partial \bar{\theta}}{\partial x} + \bar{v} \frac{\partial \bar{\theta}}{\partial y} + \bar{\omega} \frac{\partial \bar{\theta}}{\partial p} \right)^* + \nabla \cdot (\bar{\mathbf{v}}' \bar{\theta}')^* - \bar{Q}^* = 0. \quad (13)$$

Here, θ is the potential temperature, ω is the vertical pressure velocity, and Q is the diabatic heating due to

latent heat release, radiation, and other nonconservative processes. Time means are denoted with a bar. Deviations from a zonal average are denoted by an asterisk, and deviations from a time average are denoted by primes, such that $\nabla \cdot (\bar{\mathbf{v}}' \bar{\theta}')^*$ is the zonally anomalous potential-temperature-flux divergence by transient eddies. The basic state temperature gradients play a large role for this budget, and we therefore show in Fig. 6 the zonally asymmetric December–February 300-hPa temperature field \bar{T}^* onto which the forcings are added. In ALL (Fig. 6a), pronounced zonal asymmetries in temperature are present with the western coasts of continents warmer than the eastern coasts in midlatitudes. All three forcings are important for this structure.

We consider all terms in the budget [Eq. (13)] for ALL in Fig. 7 in order to establish how the various terms combine for a nearly closed budget. Zonal advection (Fig. 7a) leads to strong cooling exceeding 10 K day^{-1} off the coast of East Asia, and warming of up to 4 K day^{-1} over western North America. These temperature tendencies are due to the advection of strong zonal temperature gradients by westerly winds (Fig. 6a) in these regions. To the east of the Rockies and the Tibetan Plateau, where subsidence occurs, there is a warming tendency due to the vertical term

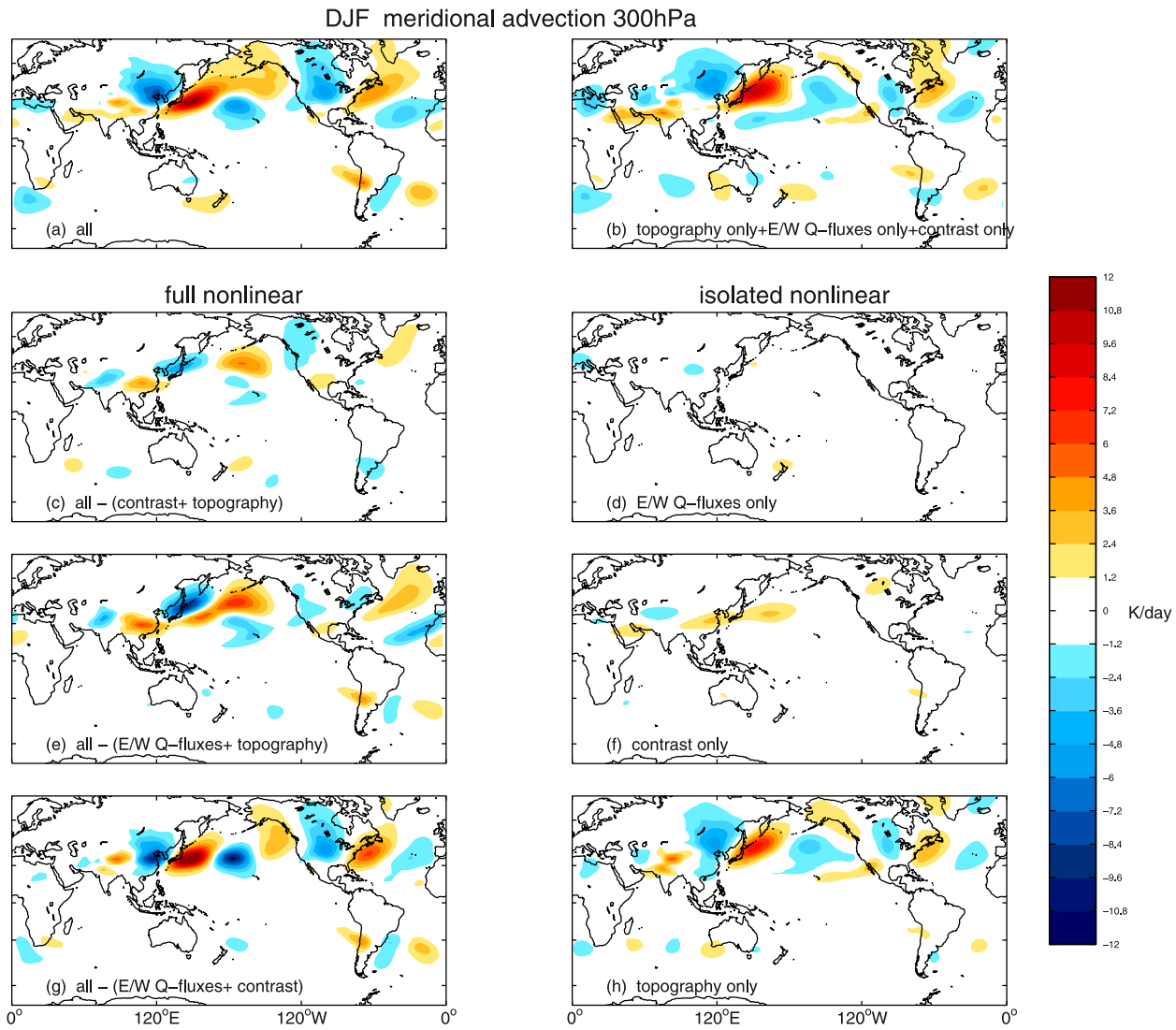


FIG. 8. As in Fig. 4, but for the meridional advection term of the thermodynamic budget. The contour interval is 1.2 K day^{-1} .

(Fig. 7c). The diabatic heating and eddy heat flux terms are small (the implications of this are discussed in the discussion section), and the meridional advection term completes the budget (Fig. 7b). In particular, there is southward advection of cold air over East Asia and northward advection of warm air over the western Pacific, both associated with the trough in the far western Pacific. Similarly, over North America, the vertical term leads to cooling over the West Coast and warming over the Plains region, while the zonal advection leads to warming over the western third of the continent. These temperature tendencies are balanced by the meridional temperature advection associated with the ridge over the Rockies. Residuals are large only over topography (Fig. 7f), where the interpolation from the model hybrid vertical coordinate to pressure coordinates impacts

the wind and temperature field. Figure S12 shows the same budget but applied to ERA5 data; the various terms in ALL and in ERA5 agree well.

We now use this budget in order to clarify why the isolated nonlinear and full nonlinear responses to individual building blocks differ. To aid in our interpretation of how the zonally anomalous steady-state thermodynamic balance can be used to illuminate the forcing of stationary waves, we rearrange the budget [Eq. (13)] as

$$\left(\bar{v} \frac{\partial \bar{\theta}}{\partial y} \right)^* = \bar{Q}^* - \left(\bar{u} \frac{\partial \bar{\theta}}{\partial x} + \bar{\omega} \frac{\partial \bar{\theta}}{\partial p} \right)^* - \nabla \cdot (\bar{\mathbf{v}} \bar{\theta})^*. \quad (14)$$

Terms on the right-hand side are interpreted here as forcings that must be balanced by changes in $\bar{\mathbf{v}}$ [see section 3 of Hoskins and Karoly (1981) and section 4a of

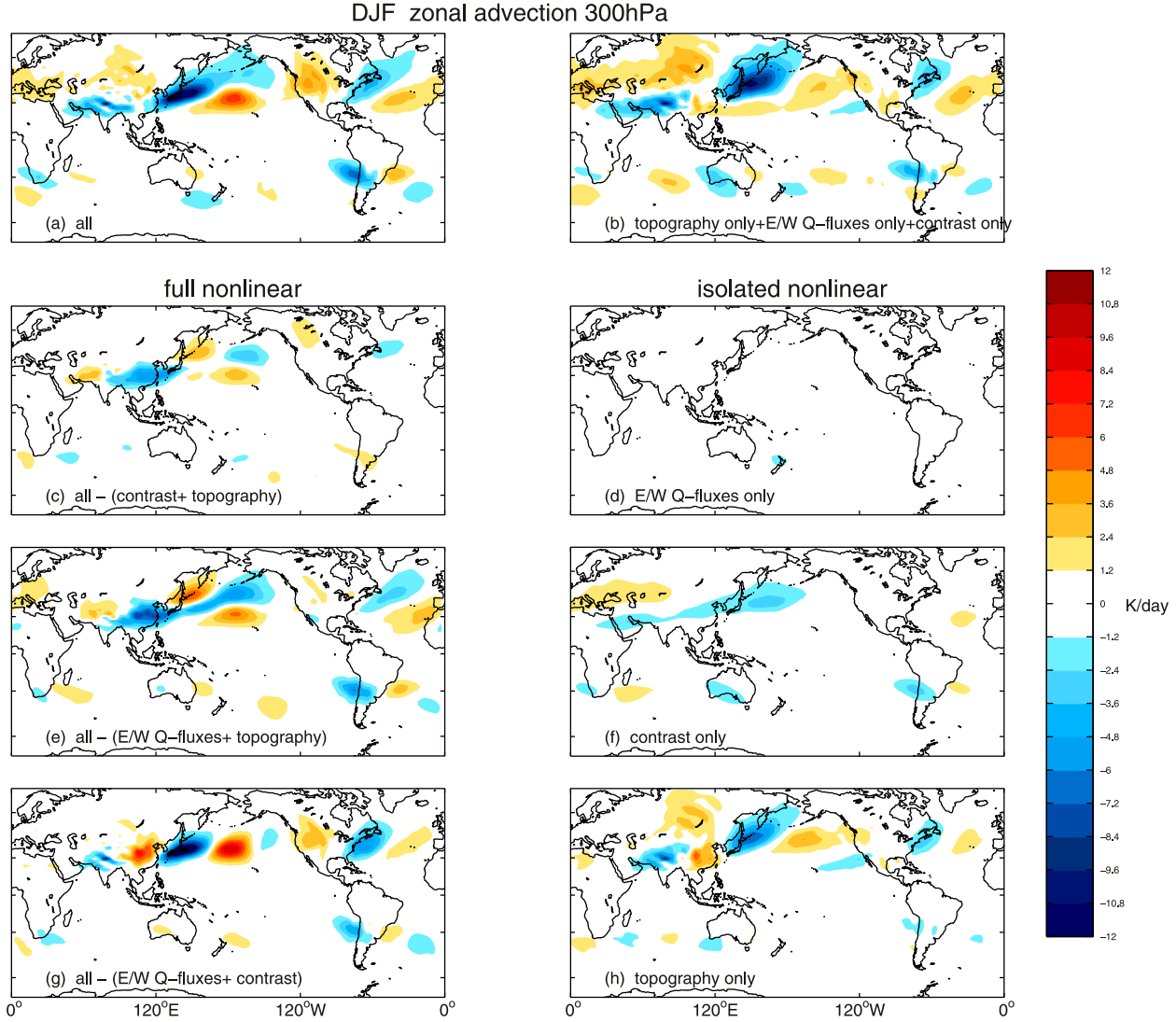


FIG. 9. As in Fig. 4, but for the zonal advection term of the thermodynamic budget. The contour interval is 1.2 K day^{-1} .

Downloaded from <http://journals.ametsoc.org/jcli/article-pdf/33/13/5611/4955256/jcli190181.pdf> by guest on 20 July 2020

Inatsu et al. (2002)]. If the sum of the terms on the right-hand side is negative, then warm air must be advected from more tropical latitudes in order to balance the budget, requiring southerly winds. On the other hand, if the sum of the terms on the right-hand side is positive, then cold air must be advected from more poleward latitudes in order to balance the budget, requiring northerly winds.

We first address why both land-sea contrast and ocean heat fluxes have a weaker impact on the northwest Pacific low in the isolated nonlinear response as compared to the full nonlinear response (Fig. 4e vs Fig. 4f and Fig. 4c vs Fig. 4d). Figures 8–10 show the meridional advection term, zonal advection term, and vertical term, respectively, for the isolated nonlinear and full nonlinear responses for each forcing.

Meridional advection leads to a cooling tendency near Japan and a warming tendency over the central Pacific in response to Q fluxes or land-sea contrast (Fig. 8c and Fig. 8e), but such a response is far weaker in the isolated nonlinear response (cf. Fig. 8c to Fig. 8d and Fig. 8e to Fig. 8f). This change in magnitude of meridional advection is consistent with the difference in strength of the low off the coast of Asia (Fig. 4), as the meridional winds associated with this low cause this meridional temperature advection. The meridional temperature advection is balanced by the zonal advection term (Figs. 9c and 9e): the stronger northwest Pacific winds associated with ocean heat flux asymmetries and land-sea contrast advect colder continental temperatures off the coast of Asia if East Asia is already cold. The background states of 300-hPa

temperature zonal gradients are shown in Figs. 6e and 6f, and include a cold continental East Asia in winter. These cold temperatures are due to the effect of the Tibetan Plateau, as even if topography is imposed in isolation the temperatures are colder over East Asia (Figs. 6c,e).² The net effect is that the meridional temperature advection term must be larger in the full nonlinear response than in the isolated nonlinear response for a closed steady-state budget, and this in turn necessitates a stronger trough in the full nonlinear response.

Why is the response to the Rockies weaker in the isolated nonlinear response as compared to the full nonlinear response (Fig. 4g vs Fig. 4h)? The zonally anomalous steady-state thermodynamic balance can again provide a diagnosis of this effect. Meridional advection leads to cooling over the Plains and warming over the far-northeastern Pacific (Figs. 8g and 8h), but such a response is far weaker in the isolated nonlinear response in Fig. 8h. This dipolar meridional advection is associated with the ridge over the Rockies, which is stronger in the full nonlinear response (Figs. 4g,h). The vertical term is similar in the isolated nonlinear and full nonlinear response, and hence does not account for this difference (Figs. 10g and 10h). Rather, the meridional temperature advection is balanced by the zonal advection term (Figs. 9g and 9h): land-sea contrast leads to a large gradient in temperatures between the east Pacific and North America (Fig. 6d), and hence there is a warming tendency over western North America. A stronger stationary wave response must exist in order to balance this warming through enhanced meridional advection.

The thermodynamic budget does not appear to explain why the full nonlinear response to topography is weaker over western Russia (Figs. 4g,h). This effect can be more directly explained by examining the lower-tropospheric winds incident on the mountains of central Asia when topography is imposed on a zonally symmetric background state versus a background state that already incorporates land-sea contrast. When land-sea contrast is included, the surface winds incident on the Tibetan Plateau are weaker due to enhanced surface drag than when land-sea contrast is not included; for example, 850-hPa zonal wind at 40°N, 65°E is 12.0 m s⁻¹ in the no-forcing integration

(experiment 0 in Table 1) and 8.1 m s⁻¹ in the integration with ocean heat flux asymmetry and land-sea contrast. (The weakenings in 850-hPa zonal wind at 45°N, 65°E and 50°N, 65°E upon including land-sea contrast are even larger: -4.9 and -4.5 m s⁻¹ respectively.) These weaker winds incident on the mountains of central Asia lead to weaker low-level rising motion and hence a weaker full nonlinear stationary wave response.

Do other budgets provide additional insight into the differences between the isolated nonlinear and full nonlinear responses? We have also computed the 200-hPa Rossby wave source as in Sardeshmukh and Hoskins (1988) for each experiment, and the results are shown in Fig. 11. The Rossby wave source in ALL is stronger than in the linear summation over East Asia and the far west Pacific. The Rossby wave source in the far western Pacific is stronger for the full nonlinear response to both east-west asymmetries and land-sea contrast as compared to the isolated nonlinear response, and hence is consistent with the stronger stationary wave response (Fig. 4e vs Fig. 4f and Fig. 4c vs Fig. 4d). We can decompose the change in Rossby wave source into the advection of absolute vorticity by the divergent wind $[-\mathbf{v}_x \cdot (\zeta + f)]$ and the direct forcing by divergence $[(\zeta + f)\nabla \cdot \mathbf{v}]$. The latter term dominates, but the former term acts as a nonnegligible negative feedback (not shown). Indeed, the pattern of upper-level divergence (Fig. S13) exhibits enhanced divergence in the subtropical far western Pacific for the full nonlinear response to east-west asymmetry and land-sea contrast as compared to the isolated nonlinear response (Fig. S13c vs Fig. S13d, and Fig. S13e vs Fig. S13f). Similar results are evident if we focus on column-averaged pressure-weighted diabatic heating (Fig. S14). We specifically note that the isolated nonlinear and full nonlinear response of diabatic heating differ both for land-sea contrast and east-west asymmetries, with the full nonlinear response exhibiting stronger zonal asymmetries. Hence, the presence or absence of topography regulates the diabatic heating field that is generated by land-sea contrast and east-west asymmetries. This nonlinearity cannot be easily accounted for in studies that impose diabatic heating as derived from observations or a comprehensive general circulation model, or that use an iterative procedure to determine the diabatic heating that leads to a realistic basic state.

The Rossby wave source over the Rockies differs between the isolated nonlinear and full nonlinear response to topographic forcing (Figs. 11g,h), and appears to act as a negative feedback as divergence over the west coast of North America is stronger in the

²The vertical term also is associated with warming of the east coast of Asia and cooling over the western Pacific (Figs. 10c,e) that is more pronounced in the full nonlinear response, although we interpret this warming of the east coast of Asia as the subsidence located to the west of a low in quasigeostrophic theory, and the low is stronger in the full nonlinear response.

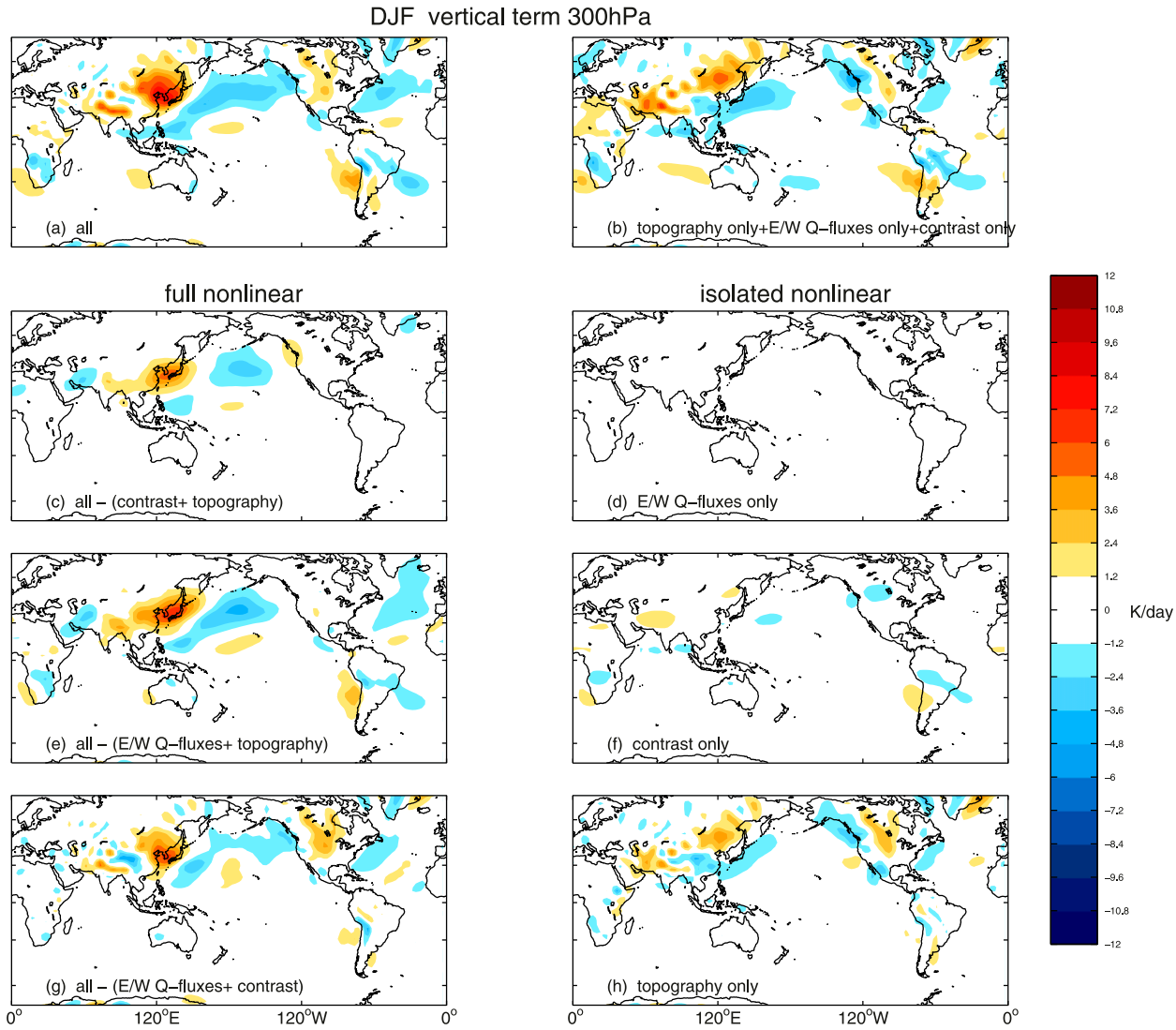


FIG. 10. As in Fig. 4, but for the vertical term of the thermodynamic budget. The contour interval is 1.2 K day^{-1} .

Downloaded from <http://journals.ametsoc.org/jcli/article-pdf/33/13/5611/4955256/jcli190181.pdf> by guest on 20 July 2020

isolated nonlinear response (Figs. S12g,h); the dynamics of this feature should be explored for future work. We have also examined the generation of stationary waves using the Plum (1985) wave activity fluxes, and while the amplitude of the fluxes differed between the isolated nonlinear and full nonlinear responses consistent with the amplitude of the stationary waves, there was no clear explanation of why such a difference may occur (not shown).

Overall, the thermodynamic budget, and to a lesser degree the Rossby wave source, allows us to diagnose why the isolated nonlinear and full nonlinear responses differ in response to each forcing. In all cases, the difference between the isolated nonlinear and full nonlinear response can be tracked down to differences in the

background state set up by the other forcings upon which a new forcing is added.

5. Sensitivity analysis for land-sea contrast and east-west asymmetry of ocean heat fluxes

We impose east-west asymmetry in ocean heat fluxes in four different oceanic regions (tropical Atlantic, tropical Pacific, extratropical Atlantic, and extratropical Pacific, as described in section 2b and shown in Fig. S1), and we now consider the relative importance of east-west asymmetry in each of these four regions for stationary waves. Figure 12a shows the eddy height field at 300 hPa and 50°N being similar to Fig. 2, except for the isolated nonlinear response to the Pacific warm pool

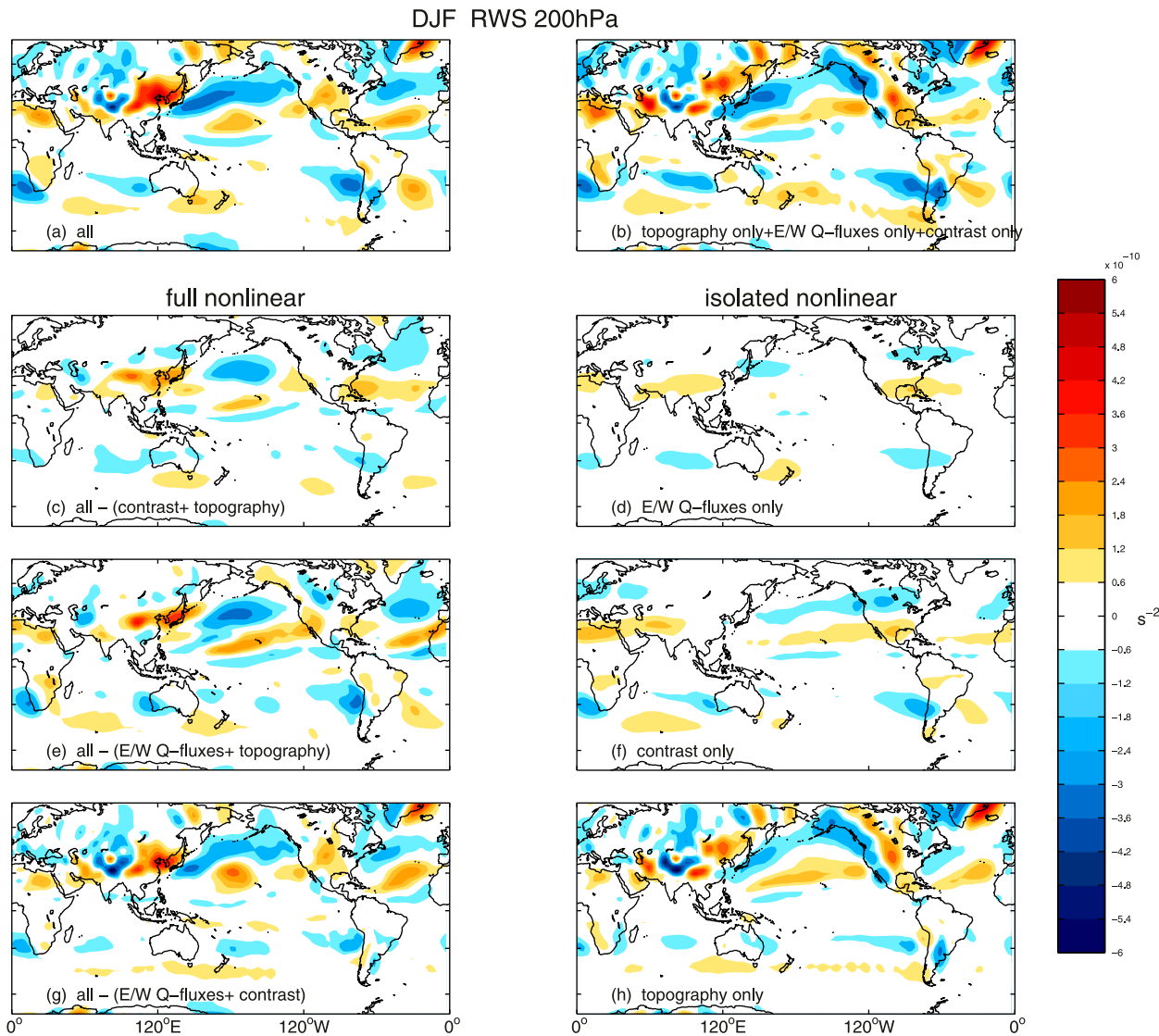


FIG. 11. As in Fig. 4, but for the Rossby wave source calculated as in Sardeshmukh and Hoskins (1988). The contour interval is $6 \times 10^{-11} \text{ s}^{-2}$.

Downloaded from <http://journals.ametsoc.org/jcli/article-pdf/33/13/5611/4955256/jcli190181.pdf> by guest on 20 July 2020

(green in Fig. 12a), the isolated nonlinear and full nonlinear response to all east–west asymmetries except the Pacific warm pool (black and gray in Fig. 12a respectively), and also when a Pacific warm pool is added to a model configuration with land–sea contrast and topography (light blue in Fig. 12a). The solid blue line is ALL, and the magenta line is repeated from Fig. 2. Over the Pacific sector, the green and magenta lines are nearly identical and both the isolated nonlinear and full nonlinear response to ocean heat fluxes in other sectors is small. Hence, perhaps expectedly, the Pacific warm pool is more important than ocean heat fluxes in the other three regions for the stationary waves in the Pacific sector. In the Atlantic sector, the Pacific warm pool is comparatively unimportant (as the green line is generally closer to

zero than the magenta line), although differences between the isolated nonlinear and full nonlinear responses to individual forcings preclude a simple interpretation as to which zonal asymmetries in ocean heat fluxes are most important.

Which aspect of land–sea contrast is most important for forcing the stationary wave pattern? Recall that we include three aspects of land–sea contrast in ALL: the difference in mechanical damping of near-surface winds between the relatively rough land surface and relatively smooth ocean, the difference in evaporation between land and ocean, and the difference in heat capacity. Figure 12b is constructed in a similar manner to Fig. 12a, and attempts to answer this question by considering the full and isolated nonlinear responses

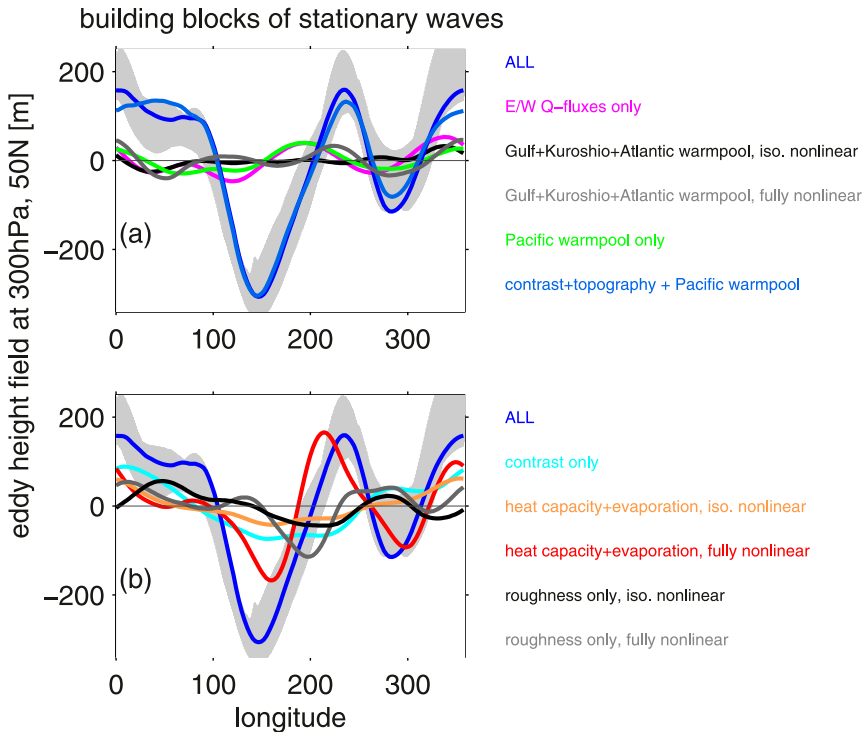


FIG. 12. As in Fig. 2, but exploring the nonlinearities in the response to (a) ocean heat fluxes and (b) land-sea contrast. The isolated nonlinear and full nonlinear responses are defined in the text.

to these three components. The isolated nonlinear response to the combined effect of heat capacity and evaporation differences between land and ocean is shown in orange, and the full nonlinear response to these same forcings is shown in red; the isolated and full nonlinear responses differ strongly. The black line show the isolated nonlinear response to land–ocean differences in damping of wind, while a gray line shows the full nonlinear response to this forcing; there are qualitative differences between the isolated and full nonlinear responses. Hence the responses to the various components of land–sea contrast differ depending on the order in which they are introduced. Stated another way, if the isolated nonlinear stationary wave response to heat capacity and evaporation (in orange) is added to the isolated nonlinear stationary wave response to roughness for mechanical dissipation (in black), one does not recover the isolated nonlinear stationary wave response when all three forcings are included (cyan; repeated from Fig. 2). We therefore are unable to draw conclusions as to which aspect of land–sea contrast is most important.

6. Discussion and conclusions

A good understanding of the mechanisms controlling stationary waves is important. First, the position and

intensity of stationary waves strongly influence surface temperatures over the populated midlatitude regions, modifying the direction of winds and hence temperature advection. Second, stationary waves influence the distribution of storm tracks and their associated extreme wind and precipitation events. Subtle shifts in the stationary waves can therefore lead to profound impacts on regional climate even if zonally averaged changes are small. To interpret and have confidence in simulated changes in the regional climate of the extratropics, it is important to have a good understanding of mechanisms for stationary waves.

In this study, we ask: can one reconstruct the full magnitude of stationary waves by adding together the individual building blocks? In the Pacific and North American sectors, the answer is resolutely no. Over the northwest Pacific/East Asia, the sum of the responses to each individual forcing is $\sim 30\%$ weaker as compared to a simulation in which all three forcings are included and interact with one another. Over the northeast Pacific and North America, the sum of the responses to each forcing is actually opposite to that when all three are imposed simultaneously [in agreement with Ting et al. (2001)]. Only over western Eurasia is linear additivity a reasonable assumption. This leads to stratospheric stationary waves that are

similarly nonadditive in the Western Hemisphere; in particular, wave 2 is twice as strong when all forcings are imposed simultaneously as compared to when each forcing is imposed individually (*Fig. 5*). Surface temperature zonal asymmetries are also nonadditive over Europe and North America.

The nonadditivity of the forcings over the Pacific sector is due to nonlinear interactions between the forcings. Specifically, the response to land-sea contrast and east-west ocean heat fluxes is qualitatively different if they are imposed on a basic state in which topography is already included [generally consistent with Park et al. (2013)]. Similarly, the response to topography is qualitatively different if it is imposed on a basic state in which land-sea contrast and east-west ocean heat fluxes are already included. The causes of this nonadditivity can be diagnosed using the zonally anomalous steady-state thermodynamic balance, and we find that the background-state temperature field set up by each forcing (and especially the zonal derivatives of the temperature field) play a crucial role in determining the strength (or even existence) of a stationary wave response to a given forcing. All three forcings considered here strongly impact the temperature field and its zonal gradients. That substantial nonlinearities exist in the formation of NH wintertime stationary waves has been recognized for more than 20 years (Ringler and Cook 1999; Ting et al. 2001; Held et al. 2002); the novelty of this work is that we can decompose the nonlinearities associated with specific forcings such as land-sea contrast, without resorting to specifying diabatic heating or sea surface temperatures. Indeed, we show in Fig. S14 that the diabatic heating associated with each forcing includes a substantial nonadditive component, and nonadditivity is also evident in the surface temperature response (*Fig. 2c*).

Despite the nonadditivity of the various forcings, there are some regions where a single forcing plays the dominant role. For example, orography is the single most important factor for Pacific sector stationary wave, while over the European sector land-sea contrast plays a larger role. While the responses to each forcing are generally additive over Europe, there are still some ambiguities even in this region. For example, if land-sea differences in momentum drag are imposed in isolation on a zonally symmetric background state, then the response is minimal and one would interpret differential momentum drag as being unimportant. However, if differential momentum drag is imposed on a background state already disturbed by orography and east-west ocean heat fluxes, then the response is nearly as strong as the full response to land-sea contrast. Such nonadditivity implies that it is not possible

to rank the relative importance of the factors in a robust manner.

In the zonally anomalous steady-state thermodynamic balance, the diabatic heating term was not found to be an important contributor to the generation of stationary waves. While at face value this may seem contrary to studies that imposed diabatic heating directly and found a strong response, we want to emphasize that diabatic heating is still crucial for the generation of stationary waves even in the context of the thermodynamic balance (albeit in an indirect manner). Namely, diabatic heating helps set up the large-scale temperature and wind fields critical for the response to the other forcing(s); that is, diabatic heating leads to the difference between *Fig. 6b* and the other panels on *Fig. 6*. Specifically, the difference between the isolated nonlinear and full nonlinear response to, for example, topography over western North America can be thought of as due to the diabatic heating pattern associated with land-sea contrast and east-west ocean heat fluxes. Similarly, eddy fluxes were found to be a negligible contributor to the generation of stationary waves in the zonally anomalous steady-state thermodynamic balance, but to the extent that eddy fluxes are important in setting up the large-scale temperature and jet structure, they also indirectly control stationary waves.

Our results have implications for studies using a linear stationary wave model. Specifically, many of these studies find substantial sensitivity as to the details of the background state about which one linearizes [see the discussion in Held et al. (2002)]. In our nonlinear MiMA simulations we find that the Pacific sector stationary wave pattern is a nonadditive response to the underlying building blocks, as a pre-existing background zonal temperature gradient allows for a qualitatively different response to a given forcing. Hence it is not surprising that a stationary wave model linearized about subtly different background states can produce qualitatively different stationary wave patterns. Our results also have implications for studies using general circulation models with imposed sea surface temperatures to study the building blocks of stationary waves. Zonal asymmetries in the surface temperature field when all forcings are imposed simultaneously differ from those when each forcing is imposed individually (*Fig. 2c*), and hence imposing sea surface temperatures could lead to misrepresenting, for example, the net impact of topography on stationary waves as sea surface temperatures should also change if Earth's topography were flat.

While the experiments performed here help inform our understanding of the atmospheric response to imposed boundary conditions, the details of how the boundary conditions are imposed are imperfect.

We do not explicitly resolve oceanic dynamics, and hence the heat transport from one oceanic region to another is imposed in an idealized manner. Specifically, the finescale structure of the Kuroshio and Gulf Stream are not imposed here, and it is conceivable that the inclusion of small-scale SST gradients may modify our results. Furthermore, the evaporation in our most realistic configuration is still too large over many continental regions, especially over deserts. In addition, the model also lacks clouds, and hence zonal asymmetries in cloud radiative fluxes are missing. Last, the convective parameterization is highly idealized. There are still biases in the stationary waves in our most realistic configuration especially over the Euro-Atlantic sector, when compared to observations, and therefore our conclusions as to the degree to which building blocks interact nonlinearly in this region should be taken with some caution. Despite these deficiencies, we want to emphasize the potential advantages of this model for scientific problems that require an idealized model with reasonable stationary waves. The model simulates stationary waves as realistic as those present in CMIP5 models, yet is flexible enough to allow for no stationary waves at all. Hence this model can be used to demonstrate that stationary waves on Earth are composed of building blocks that interact nonlinearly with one another, with the most pronounced nonadditivity evident over the Pacific and North American sectors.

Acknowledgments. CIG, IW, and ME acknowledge the support of a European Research Council starting grant under the European Union Horizon 2020 research and innovation programme (Grant Agreement 677756). EPG acknowledges support from the U.S. NSF through Grant AGS 1546585. MJ acknowledges support from the Australian Research Council (ARC) Centre of Excellence for Climate Extremes (CE170100023) and ARC Grant FL 150100035. We thank the three anonymous reviewers for their constructive comments.

REFERENCES

- Alexander, M., and T. Dunkerton, 1999: A spectral parameterization of mean-flow forcing due to breaking gravity waves. *J. Atmos. Sci.*, **56**, 4167–4182, [https://doi.org/10.1175/1520-0469\(1999\)056<4167:ASPMOF>2.0.CO;2](https://doi.org/10.1175/1520-0469(1999)056<4167:ASPMOF>2.0.CO;2).
- Beljaars, A., and A. Holtslag, 1991: Flux parameterization over land surfaces for atmospheric models. *J. Appl. Meteor.*, **30**, 327–341, [https://doi.org/10.1175/1520-0450\(1991\)030<0327:FPOLSF>2.0.CO;2](https://doi.org/10.1175/1520-0450(1991)030<0327:FPOLSF>2.0.CO;2).
- Betts, A. K., 1986: A new convective adjustment scheme. Part I: Observational and theoretical basis. *Quart. J. Roy. Meteor. Soc.*, **112**, 677–691, <https://doi.org/10.1002/qj.49711247307>.
- , and M. Miller, 1986: A new convective adjustment scheme. Part II: Single column tests using GATE wave, BOMEX, ATEX and Arctic air-mass data sets. *Quart. J. Roy. Meteor. Soc.*, **112**, 693–709, <https://doi.org/10.1002/qj.49711247308>.
- Blackmon, M. L., G. W. Branstator, G. T. Bates, and J. E. Geisler, 1987: An analysis of equatorial Pacific sea surface temperature anomaly experiments in general circulation models with and without mountains. *J. Atmos. Sci.*, **44**, 1828–1844, [https://doi.org/10.1175/1520-0469\(1987\)044<1828:AAOEPS>2.0.CO;2](https://doi.org/10.1175/1520-0469(1987)044<1828:AAOEPS>2.0.CO;2).
- Branstator, G., 1995: Organization of storm track anomalies by recurring low-frequency circulation anomalies. *J. Atmos. Sci.*, **52**, 207–226, [https://doi.org/10.1175/1520-0469\(1995\)052<0207:OOSTAB>2.0.CO;2](https://doi.org/10.1175/1520-0469(1995)052<0207:OOSTAB>2.0.CO;2).
- Brayshaw, D. J., B. Hoskins, and M. Blackburn, 2009: The basic ingredients of the North Atlantic storm track. Part I: Land–sea contrast and orography. *J. Atmos. Sci.*, **66**, 2539–2558, <https://doi.org/10.1175/2009JAS3078.1>.
- , —, and —, 2011: The basic ingredients of the North Atlantic storm track. Part II: Sea surface temperatures. *J. Atmos. Sci.*, **68**, 1784–1805, <https://doi.org/10.1175/2011JAS3674.1>.
- Broccoli, A. J., and S. Manabe, 1992: The effects of orography on midlatitude Northern Hemisphere dry climates. *J. Climate*, **5**, 1181–1201, [https://doi.org/10.1175/1520-0442\(1992\)005<1181:TEOOOM>2.0.CO;2](https://doi.org/10.1175/1520-0442(1992)005<1181:TEOOOM>2.0.CO;2).
- Chang, E. K., 2009: Diabatic and orographic forcing of northern winter stationary waves and storm tracks. *J. Climate*, **22**, 670–688, <https://doi.org/10.1175/2008JCLI2403.1>.
- , S. Lee, and K. L. Swanson, 2002: Storm track dynamics. *J. Climate*, **15**, 2163–2183, [https://doi.org/10.1175/1520-0442\(2002\)015<2163:STD>2.0.CO;2](https://doi.org/10.1175/1520-0442(2002)015<2163:STD>2.0.CO;2).
- Charney, J. G., and A. Eliassen, 1949: A numerical method for predicting the perturbations of the middle latitude westerlies. *Tellus*, **1**, 38–54, <https://doi.org/10.3402/tellusa.v1i2.8500>.
- Cionni, I., and Coauthors, 2011: Ozone database in support of CMIP5 simulations: Results and corresponding radiative forcing. *Atmos. Chem. Phys.*, **11**, 11 267–11 292, <https://doi.org/10.5194/acp-11-11267-2011>.
- Cohen, N. Y., E. P. Gerber, and O. Böhler, 2013: Compensation between resolved and unresolved wave driving in the stratosphere: Implications for downward control. *J. Atmos. Sci.*, **70**, 3780–3798, <https://doi.org/10.1175/JAS-D-12-0346.1>.
- Copernicus Climate Change Service, 2017: ERA5: Fifth generation of ECMWF atmospheric reanalyses of the global climate. Copernicus Climate Change Service Climate Data Store (CDS), accessed 19 February 2020, <https://cds.climate.copernicus.eu/cdsapp#!/dataset/reanalysis-era5-pressure-levels?tab=overview>.
- Forget, G., and D. Ferreira, 2019: Global ocean heat transport dominated by heat export from the tropical Pacific. *Nat. Geosci.*, **12**, 351–354, <https://doi.org/10.1038/s41561-019-0333-7>.
- Frierson, D. M., I. M. Held, and P. Zurita-Gotor, 2006: A gray-radiation aquaplanet moist GCM. Part I: Static stability and eddy scale. *J. Atmos. Sci.*, **63**, 2548–2566, <https://doi.org/10.1175/JAS3753.1>.
- , —, and —, 2007: A gray-radiation aquaplanet moist GCM. Part II: Energy transports in altered climates. *J. Atmos. Sci.*, **64**, 1680–1693, <https://doi.org/10.1175/JAS3913.1>.
- Garfinkel, C. I., D. L. Hartmann, and F. Sassi, 2010: Tropospheric precursors of anomalous Northern Hemisphere stratospheric polar vortices. *J. Climate*, **23**, 3282–3299, <https://doi.org/10.1175/2010JCLI3010.1>.
- Held, I. M., 2005: The gap between simulation and understanding in climate modeling. *Bull. Amer. Meteor. Soc.*, **86**, 1609–1614, <https://doi.org/10.1175/BAMS-86-11-1609>.

- , and M. Ting, 1990: Orographic versus thermal forcing of stationary waves: The importance of the mean low-level wind. *J. Atmos. Sci.*, **47**, 495–500, [https://doi.org/10.1175/1520-0469\(1990\)047<0495:OVTFOS>2.0.CO;2](https://doi.org/10.1175/1520-0469(1990)047<0495:OVTFOS>2.0.CO;2).
- , S. W. Lyons, and S. Nigam, 1989: Transients and the extratropical response to El Niño. *J. Atmos. Sci.*, **46**, 163–174, [https://doi.org/10.1175/1520-0469\(1989\)046<0163:TATERT>2.0.CO;2](https://doi.org/10.1175/1520-0469(1989)046<0163:TATERT>2.0.CO;2).
- , M. Ting, and H. Wang, 2002: Northern winter stationary waves: Theory and modeling. *J. Climate*, **15**, 2125–2144, [https://doi.org/10.1175/1520-0442\(2002\)015<2125:NWSWTA>2.0.CO;2](https://doi.org/10.1175/1520-0442(2002)015<2125:NWSWTA>2.0.CO;2).
- Hersbach, H., and D. Dee, 2016: ERA5 reanalysis is in production, *ECMWF Newsletter*, Vol. **147**, 7, <https://www.ecmwf.int/en/newsletter/147/news/era5-reanalysis-production>.
- Hoskins, B. J., and D. Karoly, 1981: The steady linear response of a spherical atmosphere to thermal and orographic forcing. *J. Atmos. Sci.*, **38**, 1179–1196, [https://doi.org/10.1175/1520-0469\(1981\)038<1179:TSLROA>2.0.CO;2](https://doi.org/10.1175/1520-0469(1981)038<1179:TSLROA>2.0.CO;2).
- , and T. Woollings, 2015: Persistent extratropical regimes and climate extremes. *Curr. Climate Change Rep.*, **1**, 115–124, <https://doi.org/10.1007/s40641-015-0020-8>.
- Iacono, M. J., E. J. Mlawer, S. A. Clough, and J.-J. Morcrette, 2000: Impact of an improved longwave radiation model, RRTM, on the energy budget and thermodynamic properties of the NCAR Community Climate Model, CCM3. *J. Geophys. Res.*, **105**, 14 873–14 890, <https://doi.org/10.1029/2000JD900091>.
- Inatsu, M., H. Mukougawa, and S.-P. Xie, 2002: Stationary eddy response to surface boundary forcing: Idealized GCM experiments. *J. Atmos. Sci.*, **59**, 1898–1915, [https://doi.org/10.1175/1520-0469\(2002\)059<1898:SERTSB>2.0.CO;2](https://doi.org/10.1175/1520-0469(2002)059<1898:SERTSB>2.0.CO;2).
- Jucker, M., 2019: The surface of an aquaplanet GCM, *Iceberg* (August 2019), <https://doi.org/10.5281/zenodo.3358284>.
- , and E. Gerber, 2017: Untangling the annual cycle of the tropical tropopause layer with an idealized moist model. *J. Climate*, **30**, 7339–7358, <https://doi.org/10.1175/JCLI-D-17-0127.1>.
- Kaspi, Y., and T. Schneider, 2013: The role of stationary eddies in shaping midlatitude storm tracks. *J. Atmos. Sci.*, **70**, 2596–2613, <https://doi.org/10.1175/JAS-D-12-082.1>.
- Kitoh, A., 1997: Mountain uplift and surface temperature changes. *Geophys. Res. Lett.*, **24**, 185–188, <https://doi.org/10.1029/96GL03953>.
- Lindberg, C., and A. J. Broccoli, 1996: Representation of topography in spectral climate models and its effect on simulated precipitation. *J. Climate*, **9**, 2641–2659, [https://doi.org/10.1175/1520-0442\(1996\)009<2641:ROTISC>2.0.CO;2](https://doi.org/10.1175/1520-0442(1996)009<2641:ROTISC>2.0.CO;2).
- Manabe, S., and T. B. Terpstra, 1974: The effects of mountains on the general circulation of the atmosphere as identified by numerical experiments. *J. Atmos. Sci.*, **31**, 3–42, [https://doi.org/10.1175/1520-0469\(1974\)031<0003:TEOMOT>2.0.CO;2](https://doi.org/10.1175/1520-0469(1974)031<0003:TEOMOT>2.0.CO;2).
- Merlis, T. M., T. Schneider, S. Bordoni, and I. Eisenman, 2013: Hadley circulation response to orbital precession. Part II: Subtropical continent. *J. Climate*, **26**, 754–771, <https://doi.org/10.1175/JCLI-D-12-00149.1>.
- Minobe, S., A. Kuwano-Yoshida, N. Komori, S.-P. Xie, and R. J. Small, 2008: Influence of the Gulf Stream on the troposphere. *Nature*, **452**, 206–209, <https://doi.org/10.1038/nature06690>.
- Mlawer, E. J., S. J. Taubman, P. D. Brown, M. J. Iacono, and S. A. Clough, 1997: Radiative transfer for inhomogeneous atmospheres: RRTM, a validated correlated- k model for the longwave. *J. Geophys. Res.*, **102**, 16 663–16 682, <https://doi.org/10.1029/97JD00237>.
- Neelin, J. D., B. Langenbrunner, J. E. Meyerson, A. Hall, and N. Berg, 2013: California winter precipitation change under global warming in the Coupled Model Intercomparison Project phase 5 ensemble. *J. Climate*, **26**, 6238–6256, <https://doi.org/10.1175/JCLI-D-12-00514.1>.
- Nigam, S., I. M. Held, and S. W. Lyons, 1986: Linear simulation of the stationary eddies in a general circulation model. Part I: The no-mountain model. *J. Atmos. Sci.*, **43**, 2944–2961, [https://doi.org/10.1175/1520-0469\(1986\)043<2944:LSOTSE>2.0.CO;2](https://doi.org/10.1175/1520-0469(1986)043<2944:LSOTSE>2.0.CO;2).
- , —, and —, 1988: Linear simulation of the stationary eddies in a GCM. Part II: The “mountain” model. *J. Atmos. Sci.*, **45**, 1433–1452, [https://doi.org/10.1175/1520-0469\(1988\)045<1433:LSOTSE>2.0.CO;2](https://doi.org/10.1175/1520-0469(1988)045<1433:LSOTSE>2.0.CO;2).
- Parfitt, R., A. Czaja, S. Minobe, and A. Kuwano-Yoshida, 2016: The atmospheric frontal response to SST perturbations in the Gulf Stream region. *Geophys. Res. Lett.*, **43**, 2299–2306, <https://doi.org/10.1002/2016GL067723>.
- Park, H.-S., S.-P. Xie, and S.-W. Son, 2013: Poleward stationary eddy heat transport by the Tibetan Plateau and equatorward shift of westerlies during northern winter. *J. Atmos. Sci.*, **70**, 3288–3301, <https://doi.org/10.1175/JAS-D-13-039.1>.
- Plumb, R. A., 1985: On the three-dimensional propagation of stationary waves. *J. Atmos. Sci.*, **42**, 217–229, [https://doi.org/10.1175/1520-0469\(1985\)042<0217:OTTDPO>2.0.CO;2](https://doi.org/10.1175/1520-0469(1985)042<0217:OTTDPO>2.0.CO;2).
- Ringler, T. D., and K. H. Cook, 1999: Understanding the seasonality of orographically forced stationary waves: Interaction between mechanical and thermal forcing. *J. Atmos. Sci.*, **56**, 1154–1174, [https://doi.org/10.1175/1520-0469\(1999\)056<1154:UTSOOF>2.0.CO;2](https://doi.org/10.1175/1520-0469(1999)056<1154:UTSOOF>2.0.CO;2).
- Sardeshmukh, P. D., and B. J. Hoskins, 1988: The generation of global rotational flow by steady idealized tropical divergence. *J. Atmos. Sci.*, **45**, 1228–1251, [https://doi.org/10.1175/1520-0469\(1988\)045<1228:TGOGRF>2.0.CO;2](https://doi.org/10.1175/1520-0469(1988)045<1228:TGOGRF>2.0.CO;2).
- Saulière, J., D. J. Brayshaw, B. Hoskins, and M. Blackburn, 2012: Further investigation of the impact of idealized continents and SST distributions on the Northern Hemisphere storm tracks. *J. Atmos. Sci.*, **69**, 840–856, <https://doi.org/10.1175/JAS-D-11-0113.1>.
- Seager, R., D. S. Battisti, J. Yin, N. Gordon, N. Naik, A. C. Clement, and M. A. Cane, 2002: Is the Gulf Stream responsible for Europe’s mild winters? *Quart. J. Roy. Meteor. Soc.*, **128**, 2563–2586, <https://doi.org/10.1256/qj.01.128>.
- Shaw, T. A., and T. G. Shepherd, 2007: Angular momentum conservation and gravity wave drag parameterization: Implications for climate models. *J. Atmos. Sci.*, **64**, 190–203, <https://doi.org/10.1175/JAS3823.1>.
- , J. Perlitz, and O. Weiner, 2014: Troposphere–stratosphere coupling: Links to North Atlantic weather and climate, including their representation in CMIP5 models. *J. Geophys. Res. Atmos.*, **119**, 5864–5880, <https://doi.org/10.1002/2013JD021191>.
- , and Coauthors, 2016: Storm track processes and the opposing influences of climate change. *Nat. Geosci.*, **9**, 656–664, <https://doi.org/10.1038/ngeo2783>.
- Shepherd, T. G., and T. A. Shaw, 2004: The angular momentum constraint on climate sensitivity and downward influence in the middle atmosphere. *J. Atmos. Sci.*, **61**, 2899–2908, <https://doi.org/10.1175/JAS-3295.1>.
- Simpson, I. R., T. A. Shaw, and R. Seager, 2014: A diagnosis of the seasonally and longitudinally varying midlatitude circulation response to global warming. *J. Atmos. Sci.*, **71**, 2489–2515, <https://doi.org/10.1175/JAS-D-13-0325.1>.
- , R. Seager, M. Ting, and T. A. Shaw, 2016: Causes of change in Northern Hemisphere winter meridional winds and regional hydroclimate. *Nat. Climate Change*, **6**, 65–70, <https://doi.org/10.1038/nclimate2783>.

- Smagorinsky, J., 1953: The dynamical influence of large-scale heat sources and sinks on the quasi-stationary mean motions of the atmosphere. *Quart. J. Roy. Meteor. Soc.*, **79**, 342–366, <https://doi.org/10.1002/qj.49707934103>.
- Smirnov, D., M. Newman, M. A. Alexander, Y.-O. Kwon, and C. Frankignoul, 2015: Investigating the local atmospheric response to a realistic shift in the Oyashio sea surface temperature front. *J. Climate*, **28**, 1126–1147, <https://doi.org/10.1175/JCLI-D-14-00285.1>.
- Thomson, S. I., and G. K. Vallis, 2018: Atmospheric response to SST anomalies. Part I: Background-state dependence, teleconnections, and local effects in winter. *J. Atmos. Sci.*, **75**, 4107–4124, <https://doi.org/10.1175/JAS-D-17-0297.1>.
- Ting, M., H. Wang, and L. Yu, 2001: Nonlinear stationary wave maintenance and seasonal cycle in the GFDL R30 GCM. *J. Atmos. Sci.*, **58**, 2331–2354, [https://doi.org/10.1175/1520-0469\(2001\)058<2331:NSWMAS>2.0.CO;2](https://doi.org/10.1175/1520-0469(2001)058<2331:NSWMAS>2.0.CO;2).
- Trenberth, K. E., Y. Zhang, J. T. Fasullo, and L. Cheng, 2019: Observation-based estimate of global and basin ocean meridional heat transport time series. *J. Climate*, **32**, 4567–4583, <https://doi.org/10.1175/JCLI-D-18-0872.1>.
- Wang, H., and M. Ting, 1999: Seasonal cycle of the climatological stationary waves in the NCEP–NCAR reanalysis. *J. Atmos. Sci.*, **56**, 3892–3919, [https://doi.org/10.1175/1520-0469\(1999\)056<3892:SCOTCS>2.0.CO;2](https://doi.org/10.1175/1520-0469(1999)056<3892:SCOTCS>2.0.CO;2).
- Wang, L., and P. J. Kushner, 2011: Diagnosing the stratosphere–troposphere stationary wave response to climate change in a general circulation model. *J. Geophys. Res.*, **116**, D16113, <https://doi.org/10.1029/2010JD015473>.
- White, R., D. Battisti, and G. Roe, 2017: Mongolian mountains matter most: Impacts of the latitude and height of Asian orography on Pacific wintertime atmospheric circulation. *J. Climate*, **30**, 4065–4082, <https://doi.org/10.1175/JCLI-D-16-0401.1>.
- Wiernga, J., 1993: Representative roughness parameters for homogeneous terrain. *Bound.-Layer Meteor.*, **63**, 323–363, <https://doi.org/10.1007/BF00705357>.
- Wills, R. C., and T. Schneider, 2018: Mechanisms setting the strength of orographic Rossby waves across a wide range of climates in a moist idealized GCM. *J. Climate*, **31**, 7679–7700, <https://doi.org/10.1175/JCLI-D-17-0700.1>.
- Wills, S. M., D. W. Thompson, and L. M. Ciasto, 2016: On the observed relationships between variability in Gulf Stream sea surface temperatures and the atmospheric circulation over the North Atlantic. *J. Climate*, **29**, 3719–3730, <https://doi.org/10.1175/JCLI-D-15-0820.1>.
- Wilson, C., B. Sinha, and R. G. Williams, 2009: The effect of ocean dynamics and orography on atmospheric storm tracks. *J. Climate*, **22**, 3689–3702, <https://doi.org/10.1175/2009JCLI2651.1>.
- Wright, J., and S. Fueglistaler, 2013: Large differences in reanalyses of diabatic heating in the tropical upper troposphere and lower stratosphere. *Atmos. Chem. Phys.*, **13**, 9565–9576, <https://doi.org/10.5194/acp-13-9565-2013>.
- Wu, Z., and T. Reichler, 2018: Towards a more Earth-like circulation in idealized models. *J. Adv. Model. Earth Syst.*, **10**, 1458–1469, <https://doi.org/10.1029/2018MS001356>.